Article

Cell Metabolism

Distinct properties of adipose stem cell subpopulations determine fat depot-specific characteristics

Graphical abstract

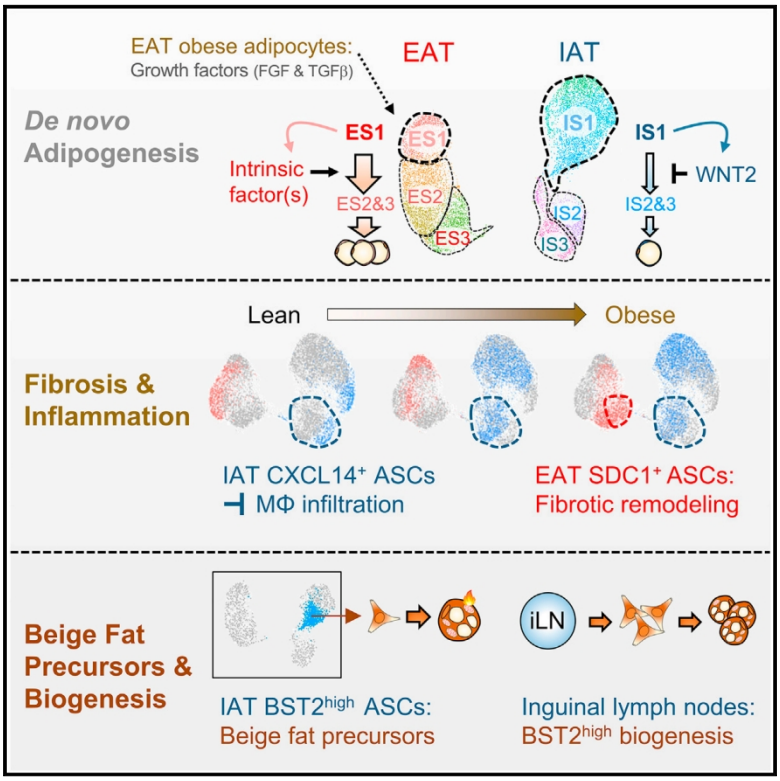

Highlights

- Single-cell RNA-seq reveals distinct ASC clusters with three adipogenic stages
- Intrinsic features of ASCs from EAT and IAT govern adipogenic potential
- SDC1^{+} and CXCL14^{+} ASCs modulate fibrosis and anti-inflammation in obesity, respectively
- IAT-specific BST2^{high} ASCs could give rise to beige adipocytes upon cold exposure

Authors

Hahn Nahmgoong, Yong Geun Jeon, Eun Seo Park, ..., Sung Hee Choi, Jong Kyoung Kim, Jae Bum Kim

Correspondence

jkkim@dgist.ac.kr (J.K.K.), jaebkim@snu.ac.kr (J.B.K.)

In brief

Using single-cell RNA-seq, Nahmgoong et al. characterize heterogeneous adipose stem cell subpopulations from normal and obese mice. They show that fat depot-specific adipose stem cell subpopulations, such as WNT2^{+}, SDC1^{+}, CXCL14^{+}, and BST2^{high} cells, are crucial for distinct metabolic features of visceral and subcutaneous white fat depots.

Nahmgoong et al., 2022, Cell Metabolism *34*, 458–472
March 1, 2022
https://doi.org/10.1016/j.cmet.2021.11.014

CellPress

CellPress

Cell Metabolism

Article

Distinct properties of adipose stem cell subpopulations determine fat depot-specific characteristics

Hahn Nahmgoong,[1,5] Yong Geun Jeon,[1,5] Eun Seo Park,[2,5] Yoon Ha Choi,[2] Sang Mun Han,[1] Jeu Park,[1] Yul Ji,[1] Jee Hyung Sohn,[1] Ji Seul Han,[1] Ye Young Kim,[1] Injae Hwang,[1] Yun Kyung Lee,[3] Jin Young Huh,[1] Sung Sik Choe,[1] Tae Jung Oh,[3] Sung Hee Choi,[3] Jong Kyoung Kim,[2,4,*] and Jae Bum Kim[1,6,*]

[1]National Creative Research Initiatives Center for Adipocyte Structure and Function, Institute of Molecular Biology and Genetics, School of Biological Sciences, Seoul National University, Seoul 08826, Republic of Korea

[2]Department of New Biology, DGIST, Daegu 42988, Republic of Korea

[3]Internal Medicine, Seoul National University College of Medicine & Seoul National University Bundang Hospital, Seoul 03080, Republic of Korea

[4]Present address: Department of Life Sciences, Pohang University of Science and Technology, Pohang 37673, Republic of Korea

[5]These authors contributed equally

[6]Lead contact

*Correspondence: jkkim@dgist.ac.kr (J.K.K.), jaebkim@snu.ac.kr (J.B.K.)

https://doi.org/10.1016/j.cmet.2021.11.014

SUMMARY

In mammals, white adipose tissues are largely divided into visceral epididymal adipose tissue (EAT) and subcutaneous inguinal adipose tissue (IAT) with distinct metabolic properties. Although emerging evidence suggests that subpopulations of adipose stem cells (ASCs) would be important to explain fat depot differences, ASCs of two fat depots have not been comparatively investigated. Here, we characterized heterogeneous ASCs and examined the effects of intrinsic and tissue micro-environmental factors on distinct ASC features. We demonstrated that ASC subpopulations in EAT and IAT exhibited different molecular features with three adipogenic stages. ASC transplantation experiments revealed that intrinsic ASC features primarily determined their adipogenic potential. Upon obesogenic stimuli, EAT-specific SDC1^{+} ASCs promoted fibrotic remodeling, whereas IAT-specific CXCL14^{+} ASCs suppressed macrophage infiltration. Moreover, IAT-specific BST2^{high} ASCs exhibited a high potential to become beige adipocytes. Collectively, our data broaden the understanding of ASCs with new insights into the origin of white fat depot differences.

INTRODUCTION

Adipose tissues store excess energy and secrete various adipokines and lipid metabolites to regulate systemic energy homeostasis (Chouchani and Kajimura, 2019; Rosen and Spiegelman, 2014). In mammals, adipose tissues are largely divided into white adipose tissue (WAT), which is specialized in energy storage, and brown adipose tissue (BAT), which produces heat to maintain body temperature. WATs are anatomically categorized into two major fat depots, visceral adipose tissue and subcutaneous adipose tissue. It has been well established that epididymal adipose tissue (EAT) and inguinal adipose tissue (IAT) are representative models of visceral and subcutaneous adipose tissues, respectively, in mice.

EAT and IAT differ in their developmental origin, anatomical location, and response to metabolic stimuli (Hwang and Kim, 2019; Tchkonia et al., 2013). EAT arises postnatally from *Wt1*$^{+}$ and *Pax3*$^{+}$ lineages, whereas IAT arises embryonically from the *Prrx1*$^{+}$ lineage (Sanchez-Gurmaches et al., 2016). EAT interacts with intra-abdominal organs, such as the gut, whereas IAT protects the body from physical stress and cold environments (Gesta et al., 2007; Tchkonia et al., 2013). Furthermore, EAT and IAT exhibit different features in response to metabolic stimuli. At the onset of obesity, EAT expands rapidly by an increasing adipocyte size (hypertrophy) and *de novo* adipogenesis (hyperplasia), whereas IAT expansion mainly depends on adipocyte hypertrophy (Jeffery et al., 2015; Wang et al., 2013). During periods of prolonged energy surplus states such as obesity, EAT exhibits fibrosis and low-grade chronic inflammation, whereas these phenomena are not largely manifested in IAT (Choe et al., 2016; Hill et al., 2018; Lee and Olefsky, 2021; Reilly and Saltiel, 2017; Saltiel and Olefsky, 2017; Sun et al., 2011). Moreover, upon exposure to cold stimuli, thermogenic beige adipocytes are produced in IAT, but not in EAT (Wang et al., 2013).

Accumulating evidence suggests that distinct properties of adipose stem cells (ASCs) would mediate different characteristics of EAT and IAT. For instance, studies using adipocytes derived from EAT or IAT ASCs have shown that these cells functionally differ in lipolysis, adipogenic potential, and thermogenic

activity (Macotela et al., 2012; Wu et al., 2012). In obesity, ASC proliferation and *de novo* adipogenesis are enhanced specifically in EAT (Jeffery et al., 2015; Wang et al., 2013). Upon cold exposure, CD81-expressing ASCs in IAT can differentiate into thermogenic beige adipocytes (Oguri et al., 2020). Furthermore, it has been reported that ASCs in IAT actively repress monocyte infiltration via secreted molecules, thereby inhibiting inflammatory responses in IAT (Hwang et al., 2019).

Recently developed single-cell RNA sequencing (scRNA-seq) analysis could deconstruct heterogeneous subpopulations, suggest cell-type-specific molecular markers, and identify potential differentiation trajectories (Choi and Kim, 2019; Kolodziejczyk et al., 2015; Stuart et al., 2019). With scRNA-seq analysis, adipogenic hierarchy and several surface markers to deconstruct ASC heterogeneity in a single fat depot have been reported (Burl et al., 2018; Ferrero et al., 2020; Gu et al., 2019; Hepler et al., 2018; Merrick et al., 2019; Oguri et al., 2020; Rajbhandari et al., 2019; Sárvári et al., 2021; Schwalie et al., 2018; Tabula Muris Consortium et al., 2018; Vijay et al., 2020). Nonetheless, as ASC clusters in EAT and IAT have not been comparatively explored in a side-by-side manner, depot-specific ASC clusters that could exhibit different features of the two fat depots are largely unknown. In addition, although there are remarkable differences in fat depots in obesity, fat depot-selective responses of ASCs to obesogenic stimuli have not been examined at a single-cell resolution. Moreover, it has not yet been thoroughly examined whether intrinsic features of ASC clusters or tissue micro-environmental factors would directly affect the adipogenic potential of EAT and IAT.

In this study, we employed scRNA-seq to comparatively characterize heterogeneous ASCs in EAT and IAT from lean and obese mice. We identified fat depot-specific ASC clusters that are important for regulation of white and beige adipocyte biogenesis. In addition, we investigated how obesogenic stimuli affect ASC characteristics and identified crucial ASC subpopulations that regulate depot-selective adipose tissue remodeling, including *de novo* adipogenesis, fibrosis, and inflammation in diet-induced obesity. Further, we examined whether intrinsic or tissue micro-environmental factors would drive the distinct features of fat depot-specific ASC clusters using ASC transplantation and lymph node (LN) dissection experiments. Collectively, our data provide a comprehensive map of ASC clusters in EAT and IAT and suggest the role of each ASC cluster to decipher distinct features of EAT and IAT upon exposure to metabolic stimuli.

RESULTS

In EAT and IAT, ASC clusters exhibit different molecular properties and comprise three adipogenic stages

To characterize ASCs in two white fat depots, Lin^- ($CD31^-$/$CD45^-$) stromal vascular fractions (SVFs) from normal chow diet (NCD)-fed mice were subjected to scRNA-seq analysis. $Msln^+$ mesothelial cells were removed from the downstream analysis to focus ASCs (STAR Methods). Unsupervised clustering analysis of 11,225 quality control-positive cells revealed ASCs from NCD mice were divided into four ASC clusters in EAT (E_N1–E_N4, N denotes NCD) and seven ASC clusters in IAT (I_N1–I_N7) (Figure 1A). It is likely that molecular features of ASC clusters in EAT and IAT were distinct, partly, due to fat depot-specific genes such as *Wt1* and *Col6a5* in EAT, and *Tbx5* and *Prrx1* in IAT (Figure 1B).

As ASCs are a heterogeneous population of cells with different adipogenic potentials (Berry and Rodeheffer, 2013; Cristancho and Lazar, 2011; Hu et al., 2019; Merrick et al., 2019; Rodeheffer et al., 2008), we inferred differentiation trajectories of the ASC clusters using Palantir (Setty et al., 2019). As shown in Figures 1C and 1D, EAT ASC clusters were largely divided into three stages: stage 1 (S1) multipotent ASCs in EAT expressing BMPs (ES1: cluster E_N1); stage 2 (S2) early committed preadipocytes in EAT highly expressing early adipogenic markers, such as *Cebpd* (ES2: clusters E_N2–E_N3); and stage 3 (S3) late committed preadipocytes in EAT expressing late adipogenic markers, such as *Fabp4* (ES3: cluster E_N4). Similarly, IAT ASC clusters were grouped into three stages: IS1 (clusters I_N1–I_N4), IS2 (cluster I_N5), and IS3 (clusters I_N6–I_N7) ASCs (Figures 1C, 1D, and S1A). A relatively small portion of smooth muscle cells, which are also able to contribute to adipocyte differentiation (Angueira et al., 2021; Shamsi et al., 2021; Tang et al., 2008), were found in E_N4 and I_N7 clusters (Figure S1B). To affirm the *in silico* adipogenic hierarchy of ASC stages, we decided to isolate and characterize ASCs in EAT and IAT by fluorescence-activated cell sorting (FACS). Among several surface markers, DPP4 was highly expressed in S1 and S2 ASCs, and ICAM1 was abundantly expressed in S2 and S3 ASCs in EAT and IAT (Figures 1E, S1C, and S1D). Sorted $DPP4^+$, $DPP4^+$/$ICAM1^+$, and $ICAM1^+$ ASCs from the two fat depots expressed S1, S2, and S3 markers (Figures 1F, S1E, and S1F), respectively, validating that DPP4 and ICAM1 seemed to be suitable markers for the isolation of S1, S2, and S3 ASCs. As expected, the extents of lipid droplet formation and adipocyte marker gene expression were higher in ES2 and ES3 ASCs than in ES1 ASCs cultured with adipogenic cocktails, whereas cell proliferation activity and osteogenic potential were higher in ES1 ASCs (Figures 1G and S1G–S1J). Similarly, IS1, IS2, and IS3 ASCs exhibited different adipogenic and osteogenic potentials (Figures 1G and S1K–S1N). Nonetheless, the gene expression profiles of the clusters comprising EAT and IAT ASCs of the three adipogenic stages were significantly different (Figure 1B), implying that the EAT and IAT ASCs in the different subpopulations may have different biological features.

One of the notable differences between EAT and IAT was that *de novo* adipogenesis was more active in EAT than in IAT in lean mice (Figures 1H and 1I). In addition, the percentage of committed preadipocytes in EAT (ES2 and ES3) was significantly higher than that in IAT (IS2 and IS3) (Figures 1F and S1O). Thus, we hypothesized that the proportion of committed preadipocytes (S2 and S3) in ASCs might be positively correlated with *de novo* adipogenesis. To address this, we examined pups and adult female mice, which have a highly enhanced capacity of *de novo* adipogenesis compared to adult male mice (Jeffery et al., 2016; Merrick et al., 2019). The proportions of S2 and S3 ASCs were higher in pups and adult female mice than in adult male mice (Figure S1P), implying that the high proportions of ES2 and ES3 ASCs indeed reflect active *de novo* adipogenesis in EAT.

Then, we explored whether analogous ASCs might be conserved in human visceral adipose tissue (VAT) from patients

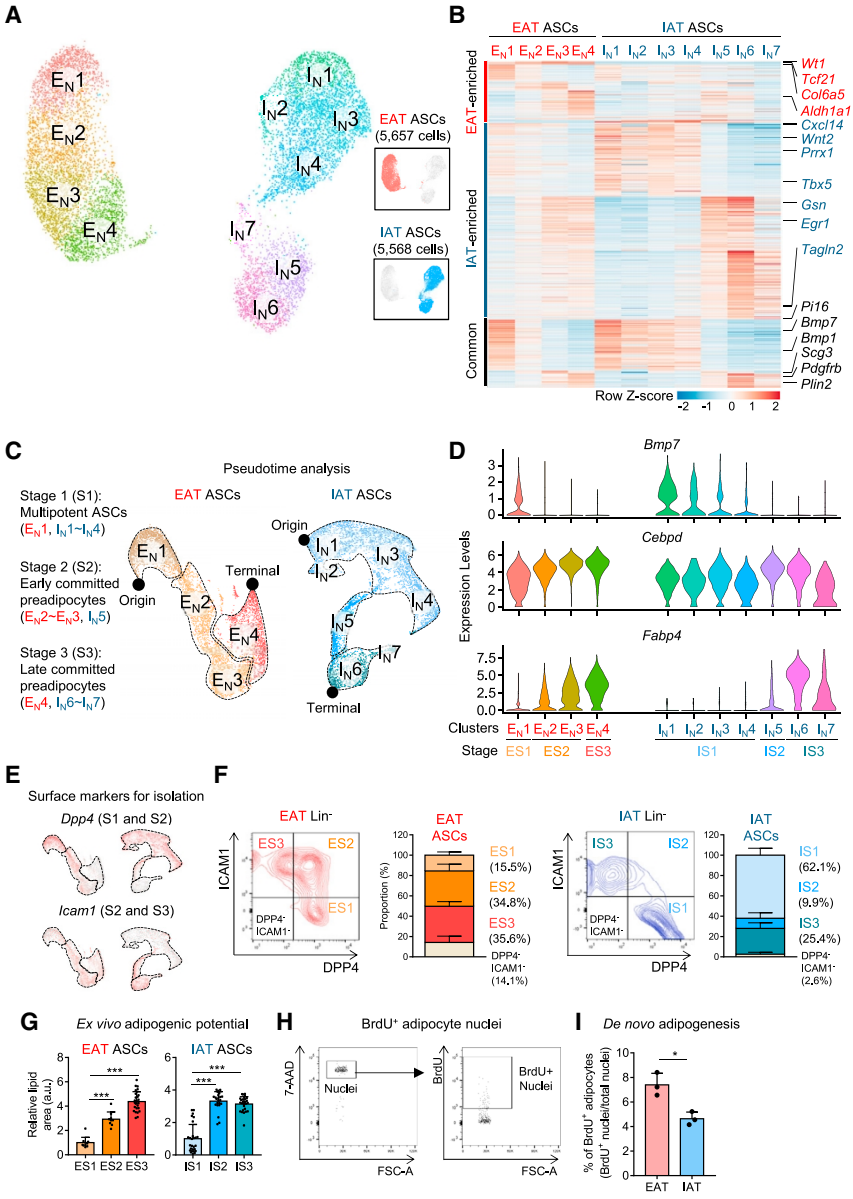

Figure 1. In EAT and IAT, ASC clusters exhibit different molecular properties and comprise three adipogenic stages

(A) Unsupervised clustering of CD31$^-$/CD45$^-$: 5,657 cells from EAT and 5,568 cells from IAT of male adult mice on a UMAP plot. Each color means separated clusters (4 clusters in EAT and 7 clusters in IAT).

(B) Heatmap showing the expression levels of fat depot-specific and common genes.

(C) *In silico* pseudotime analysis of ASCs along differentiation trajectories by using Palantir.

(D) Expression levels of stage-enriched genes.

(E) Gene expression levels of *Dpp4* and *Icam1* in EAT and IAT ASCs.

(F) Representative FACS plots and FACS-based ASC stage proportion in EAT and IAT.

(G) Quantification of lipid area in differentiated adipocytes. ASCs were differentiated for 8 days under an adipogenic condition.

(H) Representative FACS plots of BrdU$^+$ adipocyte nuclei.

(I) Quantification of BrdU incorporation into adipocyte nuclei after pulse from the first week and 9-week chase upon NCD. n = 3.

Data are represented as mean ± SD. Significance was determined using one-way ANOVA (G) and Student's t test (I). *p < 0.05, **p < 0.01, ***p < 0.001.

See also Figure S1.

with obesity. Similar to the findings in mouse EAT, the proportion of DPP4$^+$/ICAM1$^+$ S2 (40.5%) and ICAM1$^+$ S3 (38.4%) ASCs was higher than that of DPP4$^+$ S1 ASCs (12.1%) (Figure S1Q). Also, S2 and S3 ASCs in human VAT showed higher adipogenic potential and lower proliferative activity than S1 ASCs (Figures S1R–S1T), indicating that human ASCs appeared to be divided into adipogenic stages analogous to those in mice. Collectively, these data suggested that the distinct molecular properties of ASC clusters and the different proportions of ASCs in the two white fat depots would affect their adipogenic potential.

Intrinsic factors of ES1 and IS1 ASCs drive adipogenic potential

The finding that committed preadipocytes were more abundant in EAT than in IAT led us to postulate the idea that a commitment step toward preadipocytes might be differentially regulated in EAT and IAT. To address this, we isolated GFP$^+$/DPP4$^+$ ES1 and IS1 ASCs from GFP-transgenic mice and transplanted them into EAT and IAT, respectively, of wild-type mice (Figures 2A and S2A). When donor ES1 ASCs were examined, 65% of GFP$^+$ cells were found in the ES2 and ES3 populations after transplantation (Figure 2B). In contrast, 14.3% of donor IS1 ASCs were found in the IS2 and IS3 populations (Figure 2C). To investigate whether cell-intrinsic features or tissue micro-environmental factors would determine the fat depot-specific regulation of adipogenic potential, we cross-injected donor ES1 and IS1 ASCs into the opposite fat depot (Figure 2A). To our surprise, 52.2% of DPP4$^+$ donor ES1 ASCs transplanted into IAT were found in the ES2 and ES3 populations after transplantation (Figure 2D), whereas 24.3% of donor IS1 ASCs transplanted into EAT were found in the IS2 and IS3 populations (Figure 2E). These data indicated that intrinsic features of ES1 and IS1 ASCs would primarily drive commitment toward preadipocytes, whereas the fat tissue microenvironment might have a marginal effect.

To identify the cell-intrinsic factors that regulate adipogenic potential in ES1 and IS1 ASCs, we analyzed differentially expressed genes in these cells. Gene ontology analysis showed that genes enriched in ES1 ASCs, such as *Tle3* and *Egr2* (*Krox20*), were associated with fat cell differentiation (Boyle et al., 2009; Villanueva et al., 2011), whereas genes enriched in IS1 ASCs were related to cold-induced thermogenesis and

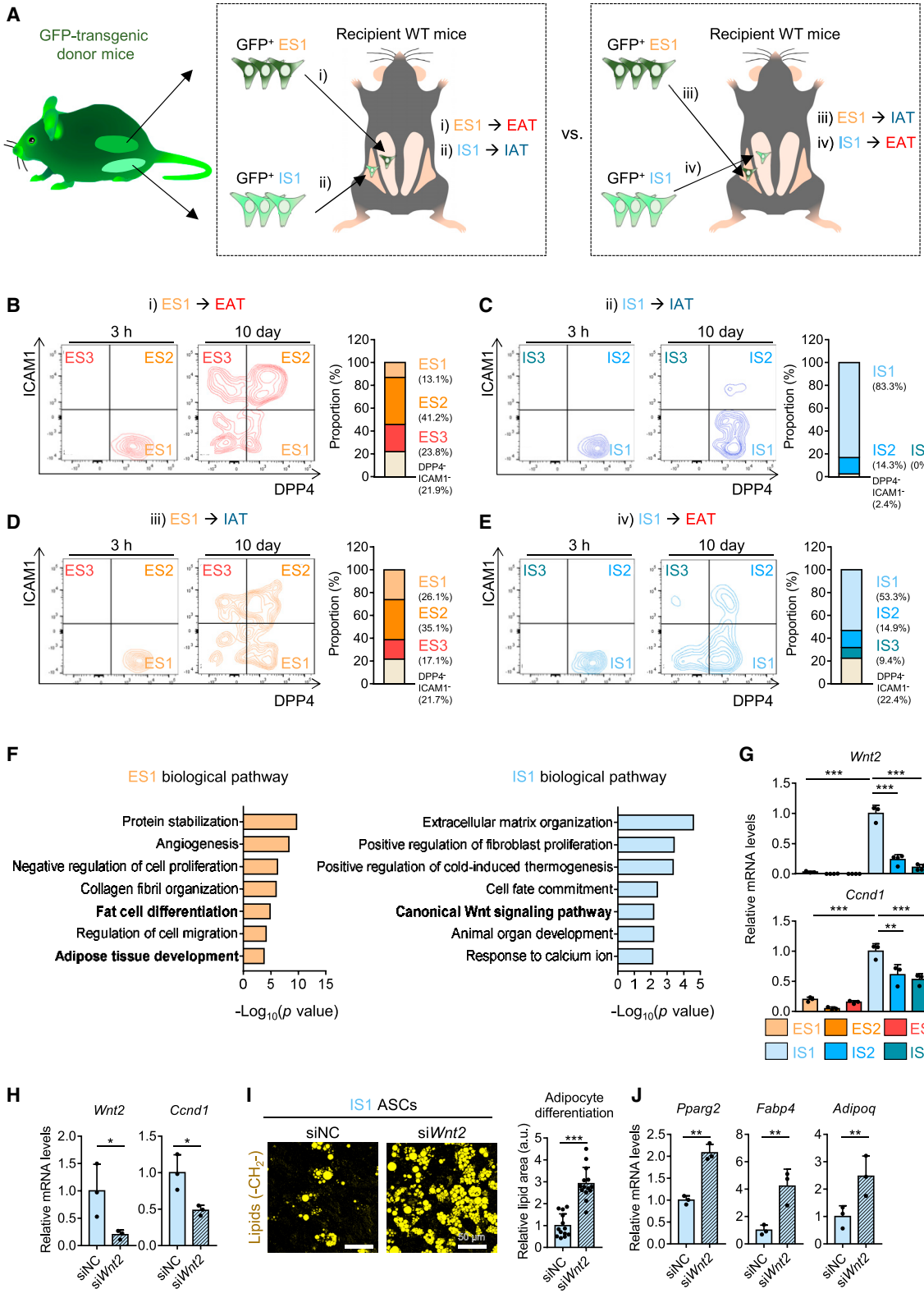

Figure 2. Intrinsic factors of ES1 and IS1 ASCs drive adipogenic potential

(A) Experimental design for ASC transplant experiments. Sorted GFP$^+$/DPP4$^+$ ES1 and IS1 ASCs were transplanted into EAT or IAT.

(B–E) Representative FACS plots and proportion of transplanted GFP$^+$/DPP4$^+$ donor cells in recipient WT mice.

(F) Gene ontology of ES1- and IS1-enriched genes.

(legend continued on next page)

canonical WNT signaling (Figures 2F, 2G, and S2B–S2D). As WNT signaling inhibits adipogenesis of mesenchymal stem cells (Christodoulides et al., 2009; Ross et al., 2000), we decided to evaluate whether *Wnt2*, the most strongly expressed WNT family gene in IS1 ASCs (Figure S2E), might suppress commitment to preadipocytes in IAT. When *Wnt2* expression was suppressed in IS1 ASCs using siRNA, lipid content and adipogenic marker gene expression were greatly enhanced in differentiated adipocytes (Figures 2H–2J). In contrast, suppression of *Wnt2* in ES1 ASCs did not significantly affect adipogenic potential (Figures S2F–S2H), implying that *Wnt2* would affect adipogenesis in a depot-specific manner. In this regard, expression quantitative trait loci related to the waist-to-hip ratio, a surrogate of visceral versus subcutaneous adipose tissue expansion in humans, were found to exist in the promoter/enhancer regions of *WNT2* and *CCND1* (Figure S2I). Taken together, these results suggested that intrinsic features would predominantly regulate the adipogenic potential of ES1 and IS1 ASCs, and WNT signaling in IS1 ASCs would restrain commitment toward preadipocytes.

In EAT, obesogenic stimuli promote ES1 ASC proliferation via FGF and TGFβ signaling to induce *de novo* adipogenesis

We and others have shown that ASCs contribute to fat depot-selective remodeling process in obesity (Hwang et al., 2019; Tchkonia et al., 2013). Upon high-fat diet (HFD), *de novo* adipogenesis was stimulated specifically in EAT (Figures S3A and S3B), consistent with previous findings (Jeffery et al., 2015; Wang et al., 2013). However, the key ASC cluster(s) and underlying molecular mechanisms mediating EAT-specific *de novo* adipogenesis in obesity are largely unknown. To tackle these issues, we characterized and compared ASC clusters in EAT and IAT using combined scRNA-seq datasets from NCD-fed, 2-week HFD-fed, and 10-week HFD-fed mice (Figure 3A). As we used unsupervised analysis, the exact cluster corresponding to the previously defined clusters E_N1–4 and I_N1–7 could not be annotated in the combined scRNA-seq dataset; however, most cells of the E_N1 cluster were found in cluster $E_{NH}1$ (NH denotes merged NCD and HFD datasets), E_N2–3 clusters in $E_{NH}2$, E_N4 cluster in $E_{NH}3$, I_N1–4 clusters in $I_{NH}1$, I_N5 cluster in $I_{NH}2$, and I_N6–7 clusters in $I_{NH}3$ cluster. Upon HFD, 8 ASC clusters in EAT ($E_{NH}4$–11) and 10 clusters in IAT ($I_{NH}4$–13) newly emerged (Figure 3A). With regard to adipogenesis, cells in the new clusters $E_{NH}4$–6 expressed ES1 markers, cells in $E_{NH}7$–9 expressed ES2 markers, and cells in $E_{NH}10$–11 expressed ES3 markers (Figure 3A). Similarly, clusters $I_{NH}4$–9 were classified as IS1, clusters $I_{NH}10$–11 as IS2, and clusters $I_{NH}12$–13 as IS3 (Figure 3A). Although the expression of several genes was altered by HFD feeding (Figure S3C), there were no significant differences in adipogenic gene expression and *ex vivo* adipogenic potential of S1, S2, and S3 ASCs in both fat depots in obesity (Figures 3B–3D, S3D, and S3E).

Notably, the proportion of ES1 ASCs was increased at the onset of obesity, and ES3 ASCs were sequentially expanded after 10-week HFD (Figures 3E and S3F). Also, after a 3- or 7-day HFD, the total number of ES1 ASCs was significantly elevated, probably due to cell proliferation (Figures 3F and 3G). To examine how ES1 ASCs would be proliferated by HFD, ES1 ASCs were incubated in conditioned media (CM) from EAT adipocytes or SVFs from mice of the NCD and 3-day HFD groups (Figure S3G). ES1 ASC proliferation was promoted by HFD-CM from adipocytes, but not SVFs, containing heat-sensitive molecules, such as growth factors (Figures S3H and S3I). Transcriptome analyses of adipocytes from mice fed an NCD or a 3-day HFD (Kim et al., 2015) indicated that the expression of several growth factors, including FGFs, TGFβ, BMPs, GDFs, and PDGFs, would be increased upon 3-day HFD (Figure 3H). To identify potential signaling molecule(s) contributing to the ES1-specific proliferation at the onset of obesity, we sought the "ligand-receptor" relationships between ligands from obese adipocytes and receptors enriched in ES1 ASCs. The results suggested that FGF and TGFβ signaling(s) may mediate the proliferation of ES1 ASCs after 3 days of HFD, which was validated using *Fgfr1* and *Tgfbr2* knockdown in ES1 ASCs (Figure 3I). Unlike in EAT, we found no significant proportion changes in IS1, IS2, or IS3 during HFD feeding periods or in the proliferation of IAT ASCs upon a 3-day HFD (Figures 3J and S3J).

To further examine whether responsiveness of ASCs or micro-environmental factors would determine the fat depot-specific ASC proliferation upon HFD, ES1 and IS1 ASCs were treated with CM from EAT or IAT adipocytes (Figure S3K). CM from EAT adipocytes with HFD enhanced proliferation of ES1 and IS1 ASCs, in which receptors for FGFs and TGFβ were highly expressed (Figures S3L and S3M). On the contrary, IAT adipocytes with HFD did not enhance proliferation of both ES1 and IS1 ASCs (Figure S3L), implying that tissue micro-environmental factors including FGFs and TGFβ secreted from EAT adipocytes might upregulate ASC proliferation at the onset of obesity. Together, these data propose that EAT-specific adipogenesis upon HFD would be potentiated by proliferation of ES1 ASCs mediated, at least in part, by FGF and TGFβ signaling cascades.

In obesity, EAT-specific SDC1$^+$ and IAT-specific CXCL14$^+$ ASCs regulate fibrosis and inflammation in a depot-specific manner

In obesity, EAT rapidly undergoes fibrosis and inflammation. Given that ASCs highly express fibrotic genes such as collagens compared to adipocytes, immune cells, and endothelial cells (Figures S4A–S4C), we attempted to identify key EAT ASC subpopulations that would mediate fibro-inflammatory features in obesity. As shown in Figure 4A, pseudotime analysis revealed

(G) mRNA levels of *Wnt2* and *Ccnd1* in EAT and IAT ASC stages. n = 3.
(H) mRNA levels of *Wnt2* and *Ccnd1* of IS1 ASCs with siRNA for negative control (NC) or *Wnt2*. n = 3.
(I) Left: representative images of differentiated adipocytes from IS1 ASCs with siRNA for negative control (NC) or *Wnt2*. Right: quantification of lipid area in differentiated adipocytes. ASCs were differentiated for 8 days under an adipogenic condition. Scale bar, 50 μm.
(J) mRNA levels of adipocyte markers in differentiated adipocytes from IS1 ASCs. n = 3.
Data are represented as mean ± SD. Significance was determined using one-way ANOVA (G) or Student's t test (H–J). *p < 0.05, **p < 0.01, ***p < 0.001.
See also Figure S2.

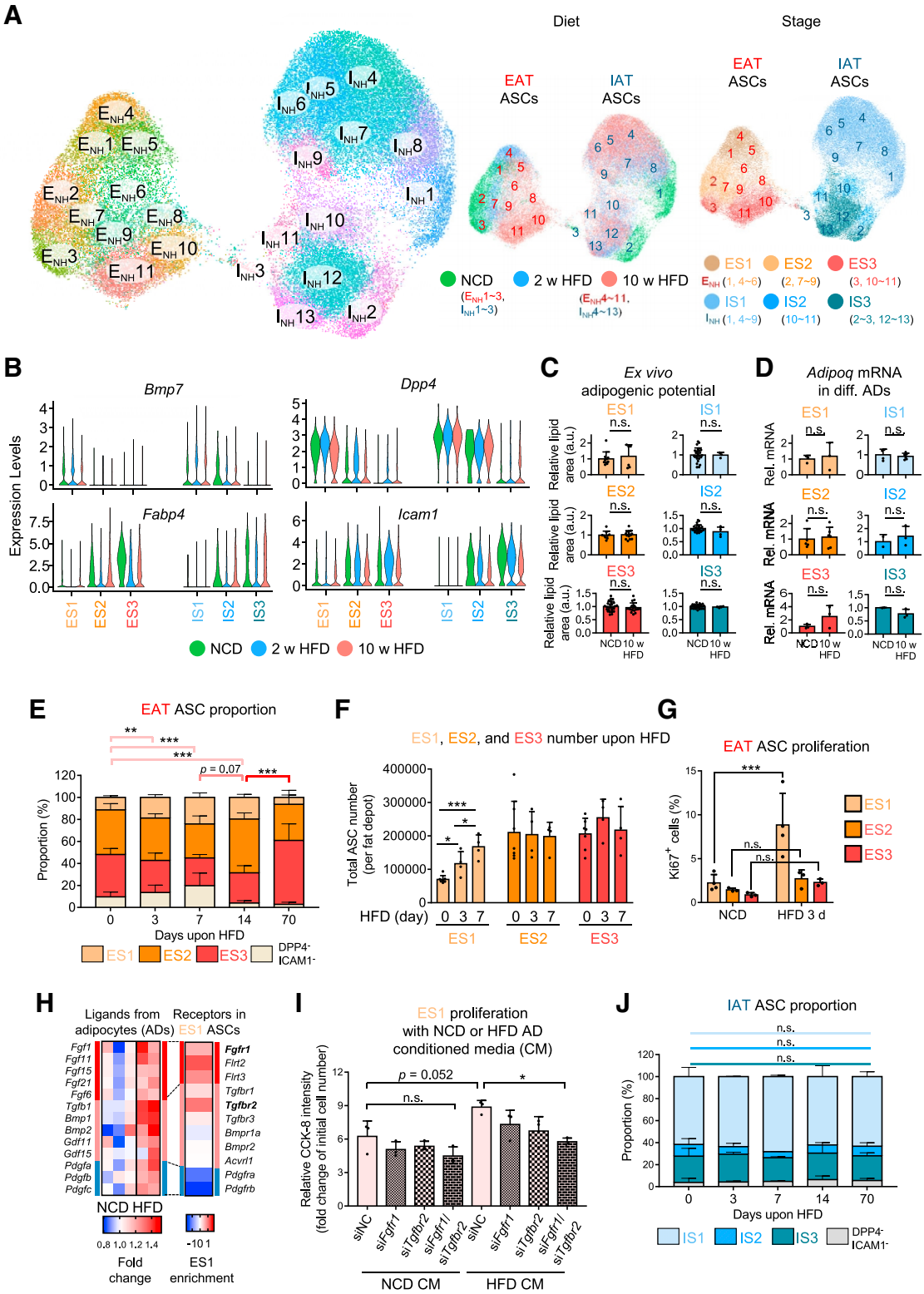

Figure 3. In EAT, obesogenic stimuli promote ES1 proliferation via FGF and TGFβ signaling to induce *de novo* adipogenesis

(A) Unsupervised clustering of CD31$^-$/CD45$^-$ ASCs from EAT and IAT of NCD-, 2-week, or 10-week HFD-fed mice.

(B) Gene expression levels of *Bmp7*, *Dpp4*, *Fabp4*, and *Icam1* in EAT and IAT ASC stages.

(C) Quantification of lipid area in differentiated adipocytes. ASCs were differentiated for 8 days under an adipogenic condition.

(legend continued on next page)

that there appeared to be two different fates of EAT ASCs in obesity. Also, independent pseudotime analysis consistently showed two fates of EAT ASCs in obesity (Figure S4D). The terminus of EAT Fate 1 with the $E_{NH}10$ cluster, presented only after a 10-week HFD, highly expressed genes related to extracellular matrix organization and inflammation, such as *Col1a1*, *Ccn2* (*CTGF*), and *Ccl2* (*MCP1*) (Figures 4B and 4C). Pathway analysis showed that TGFβ signaling would be enhanced in the terminus of EAT Fate 1 (Figure 4D). In the $E_{NH}10$ fibro-inflammatory cluster, surface marker syndecan 1 (*Sdc1*) was abundantly expressed (Figure 4E). In line with the scRNA-seq results, FACS experiments showed that $SDC1^+$ ASCs were predominant in EAT upon HFD feeding (Figure 4F). Also, further analyses proposed that the fibro-inflammatory $SDC1^+$ ASCs appeared to be a subpopulation of $CD9^+$ ASCs (Figures S4E and S4F). As $CD9^+$ ASCs are known as pro-fibrogenic cells in EAT (Hepler et al., 2018; Marcelin et al., 2017), these data postulated that $SDC1^+$ ASCs might mediate fibro-inflammatory features of $CD9^+$ ASCs. At the end of EAT Fate 2, with clusters $E_{NH}3$ and $E_{NH}11$, adipocyte differentiation-related genes, such as *Cebpd*, *Igf1*, and type IV collagens (Hu et al., 2015; Sillat et al., 2012), were enriched (Figures 4B, S4G, and S4H), implying that EAT Fate 2 would reflect the adipogenic pathway. In contrast, pseudotime analysis of IAT ASCs revealed that, unlike EAT ASCs, IAT ASCs did not branch into different fates upon obesogenic stimuli (Figure S4I). Thus, these data suggested that EAT-specific $SDC1^+$ fibro-inflammatory ASCs would contribute to EAT-selective fibro-inflammatory remodeling in obesity.

Unlike EAT, IAT exhibited relatively low-level inflammatory responses in obesity (Figures S4J and S4K). It has been recently reported that certain factors secreted from IAT ASCs could suppress monocyte infiltration (Hwang et al., 2019). To identify potential anti-inflammatory factor(s), we compared cytokine expression profiles of EAT and IAT ASCs. Compared to EAT ASCs, several IAT ASCs selectively expressed CXCL14 (Figures 4G–4I), which has been reported to act as an anti-inflammatory factor by inhibiting the CXCL12-CXCR4 pathway during monocyte migration (Figures S4L–S4N) (Tanegashima et al., 2013). In HFD-fed mice, CXCL12 expression was higher in EAT than in IAT (Figure 4J). Also, the degree of monocyte infiltration was further elevated in CM from HFD EAT than CM from HFD IAT (Figure 4K). To test whether CXCL14 might indeed be involved in monocyte migration, CXCL14 peptides were incubated in CM from EAT and IAT from HFD-fed mice. We observed that CXCL14 peptides actively repressed monocyte migration via, at least partly, suppressing the CXCL12-CXCR4 axis (Figures 4K and 4L), and knockdown of *Cxcl14* in IAT ASCs increased monocyte migration (Figures 4M and 4N). In addition, experiments with pharmacological inhibitors showed that ERK signaling would be involved in CXCL12-CXCR4-mediated monocyte migration (Figures S4O and S4P). Further, suppression of *Cxcl14* in IAT, using *in vivo* siRNA injection (Nguyen et al., 2021), greatly elevated monocyte infiltration upon HFD (Figures 4O, 4P, S4Q, and S4R). Together, these data propose that high expression of CXCL14 in IAT ASCs could repress pro-inflammatory responses in obese IAT, probably by suppressing CXCL12 activity, which can partly explain the fat-depot differences in innate immunity in obesity. Therefore, these findings suggested that fat depot-specific ASCs, such as $SDC1^+$ and $CXCL14^+$ cells, would modulate fibro-inflammatory features in a depot-specific manner in obesity.

IAT-specific $BST2^{high}$ ASCs are beige adipocyte precursors whose biogenesis is regulated by LNs

It has been suggested that beige adipocyte precursors in IAT appear to be different from classical white adipocyte precursors (Chen et al., 2019; Inagaki et al., 2016; Shapira and Seale, 2019; Wang and Seale, 2016; Wu et al., 2012; Yoneshiro et al., 2019). Given that beige adipocytes are hardly observed in EAT, we postulated that beige adipocyte precursors would be rarely present in EAT ASCs, and differentiation pathways of beige adipocyte precursors might differ from white adipocyte differentiation. To identify the IAT-specific beige adipocyte precursors, we conducted a projection analysis in which EAT ASCs were projected onto similar IAT ASCs (Figure 5A). This comparative analysis showed that cluster E_N1 was projected onto clusters I_N1–3, clusters E_N2–3 projected onto cluster I_N5, and cluster E_N4 projected onto clusters I_N6–7 (Figure 5A). Notably, there appeared to be no EAT clusters that projected onto cluster I_N4 (Figure 5A). An independent analysis using batch correction corroborated that cluster I_N4 was distinct from the other IAT and EAT clusters (Figure S5A). Cells in the IAT-specific I_N4 cluster highly expressed *Tmem26* and *Il33*, which are related to beige adipocytes (Brestoff et al., 2015; Wu et al., 2012) (Figures 5B and 5C). In addition, cells in cluster I_N4 seemed to have a differentiation fate distinct from that of other IAT ASCs (Figure 5D). To affirm that IAT-specific cluster I_N4 would exhibit beige adipocyte precursor features, we tried to isolate and characterize these ASCs by FACS. The IAT-specific cluster I_N4 abundantly expressed the surface marker *Bst2* (Figure 5E). Consistent with the

(D) mRNA levels of *Adipoq* in the differentiated adipocytes of ASCs from NCD- and 10-week HFD-fed mice. n = 2∼6.
(E) Proportion of ES1, ES2, and ES3 ASCs. Brackets with different colors indicate the statistical differences between ES1, ES2, and ES3 ASCs. n = 4∼7.
(F) Total ES1, ES2, and ES3 cell numbers from NCD-, 3-, and 7-day HFD-fed mice. n = 4∼7.
(G) Quantification of Ki67-positive cells in ASC in EAT of NCD- and 3-day HFD-fed mice. n = 3.
(H) The ligand-receptor relationship between EAT adipocyte and ES1. Expression levels of ligand were analyzed from NCD- and 3-day HFD-fed mice (GEO: GSE65557). ES1 enrichment score was calculated as fold of ES1 expression level compared to ES2 and ES3.
(I) Quantification of cell proliferation of ES1 cultured with conditioned media (CM) from primary EAT adipocytes. ES1 was transfected with siRNA for *Fgfr1* and *Tgfbr2* before CM treatment. n = 3.
(J) Proportion of IS1, IS2, and IS3 ASCs. Brackets with different colors indicate the statistical differences between IS1, IS2, and IS3 ASCs. n = 2∼16.
The number of analyzed cells is as follows: EAT NCD, 5,657; EAT 2-week HFD, 5,398; EAT 10-week HFD, 8,766; IAT NCD, 5,568; IAT 2-week HFD, 14,256; IAT 10-week HFD, 15,703.
Data are represented as mean ± SD. Significance was determined using Student's t test (C and D) or one-way ANOVA (E–G, I, and J). *$p < 0.05$, **$p < 0.01$, ***$p < 0.001$; n.s., non-significant.
See also Figure S3.

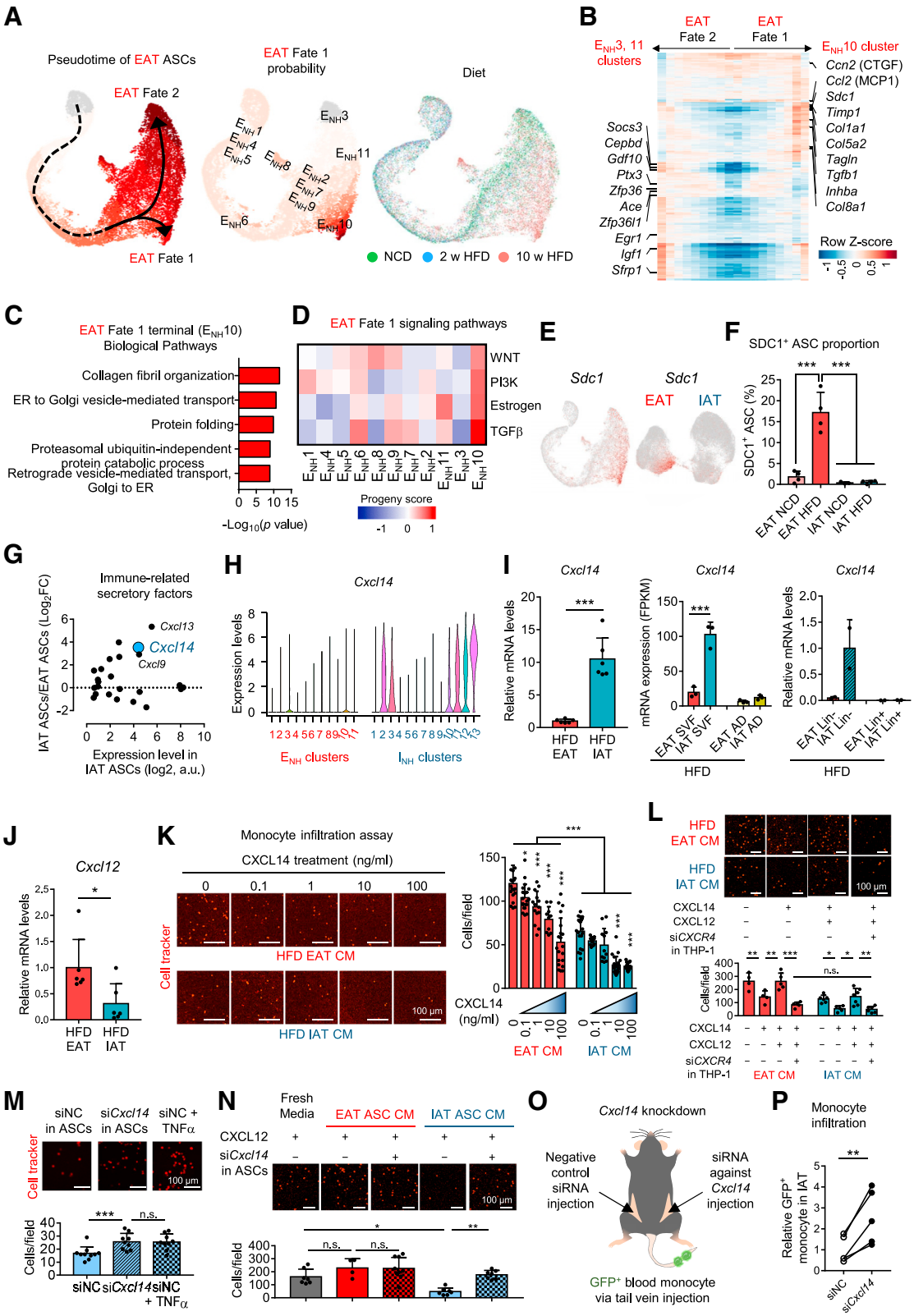

Figure 4. In obesity, EAT-specific SDC1$^+$ and IAT-specific CXCL14$^+$ ASCs regulate fibrosis and inflammation in a depot-specific manner

(A) *In silico* pseudotime analysis and EAT Fate 1 probabilistic analysis of EAT ASCs from NCD, 2-week HFD, and 10-week HFD-fed mice. Pseudotime (arbitrary units) is depicted from white to red.

(legend continued on next page)

scRNA-seq data, BST2^{high} ASCs were abundantly detected in IAT, whereas BST2^{high} ASCs were barely observed in EAT (Figures 5F, 5G, and S5B). As BST2^{high} ASCs largely expressed cluster I_N4 markers such as *Il33* and *Tmem26* (Figures 5H and S5C), it seemed that BST2 would be a suitable marker for isolating cluster I_N4. Although differentiated adipocytes from BST2^{high} ASCs highly expressed *Ucp1* and *Dio2* compared to those from BST2^{low} ASCs, the mRNA level of adipocyte marker genes and lipid accumulation were comparable between differentiated adipocytes from BST2^{high} and BST2^{low} ASCs (Figures 5I and S5D–S5F). Moreover, the proportion of BST2^{high} ASCs was increased by cold exposure, whereas that of BST2^{high} ASCs was downregulated in HFD-fed mice in which *Ucp1* expression was dampened (Figures 5J, 5K, S5G, and S5H), implying that BST2^{high} ASCs might be important to modulate *in vivo* beige fat formation in IAT upon metabolic stimuli. Together, these results suggested that IAT-specific ASC subpopulations, distinct from EAT and other IAT ASCs, can differentiate into beige adipocytes, and the beige adipocyte precursors could be sorted based on the cell surface marker, BST2.

Notably, we found that *Cxcl13* and *Pdpn*, associated with the development of ASCs into LN fibroblastic reticular cells (Bénézech et al., 2012; van de Pavert et al., 2009), were also highly expressed in I_N4 cells (Figure 5L). As LN is found in IAT, but not EAT, we asked whether IAT-specific I_N4 cells might be present near LN. To test this, we anatomically divided IAT into peri-LN IAT (PL-IAT) and distal-LN IAT (DL-IAT) (Figure 5M). As shown in Figure 5N, the proportion of BST2^{high} ASCs in total ASCs was significantly higher in PL-IAT than in DL-IAT. *Ucp1* mRNA expression was also higher in PL-IAT, accompanied by an enrichment of multilocular adipocytes, at room temperature and after cold exposure (Figures 5O, 5P, and S5I–S5K). The spatial relationship between BST2^{high} ASCs and LNs led us to investigate the roles of LNs in biogenesis of BST2^{high} beige adipocyte precursors, using LN dissection (Figure 5Q). Although it is still possible that LN dissection might induce surgical damages in IAT, it seemed that LN dissection did not significantly affect sympathetic nerve innervation in PL-IAT (Wang et al., 2019) (Figure S5L). Further, LN removal decreased the proportion of BST2^{high} ASCs in IAT (Figure 5R), implying that the LN would regulate formation of beige adipocyte precursors. Accordingly, LN removal reduced UCP1 expression in IAT and dampened the induction of UCP1$^+$ beige adipocytes at room temperature and upon exposure to cold as well as upon β3-adrenergic agonist CL316,243 treatment (Figures 5S and S5M–S5R). In humans, it has been reported that UCP1 and thermogenic gene expression levels were, unexpectedly, high in VAT (Zuriaga et al., 2017), in which lymphatic vessels are highly developed, compared to SAT (Redondo et al., 2020). In line with these, our analysis of human VAT and SAT showed that *UCP1* expression was high in human VAT compared to SAT, accompanied by relatively high expression of *TMEM26*, *IL33*, *BST2*, *CXCL13*, and *PDPN* in VAT compared to SAT (Figure S5S). Taken together, these data propose that IAT-specific BST2^{high} ASCs would give rise to beige adipocytes, and LN might regulate the thermogenic features of IAT through, at least in part, biogenesis of IAT-specific BST2^{high} beige adipocyte precursors.

DISCUSSION

In mice, EAT and IAT have a similar appearance and lipid storage function as WAT. However, emerging evidence suggests that EAT and IAT have distinct roles in the regulation of energy homeostasis (Gesta et al., 2007; Hwang and Kim, 2019; Tchkonia et al., 2013). Furthermore, human epidemiological studies have shown that the anatomical distribution of fat tissues, rather than whole-body fat mass, is critical in metabolic syndromes (Pischon et al., 2008; Shungin et al., 2015).

In this study, we analyzed EAT and IAT ASCs in response to metabolic stimuli at the single-cell resolution. Several lines of evidence suggest that the distinct properties of ASC subpopulations determine the fat depot-specific features. First, side-by-side comparison and transplantation experiments demonstrated that the intrinsic features of DPP4$^+$ ES1 and IS1 ASCs would

(B) Split heatmap of upregulated genes along EAT Fate 1 or Fate 2.
(C) Gene ontology of E_{NH}10 cluster-enriched genes.
(D) Pathway analysis of upregulated genes along with EAT Fate 1.
(E) Gene expression levels of *Sdc1*.
(F) Proportion of SDC1$^+$ cells from NCD- and 15-week HFD-fed mice. n = 3∼4.
(G) Differentially expressed genes of immune-related secretory factors (CCLs, CXCLs, and ILs) in EAT and IAT ASCs.
(H) A violin plot showing *Cxcl14* expression levels in ASC clusters from EAT and IAT of NCD-, 2-week, or 10-week HFD-fed mice.
(I) mRNA levels of *Cxcl14*. Left: EAT and IAT from 10-week HFD-fed mice. n = 5. Center: FPKM value in SVFs and adipocyte (AD) fraction from 10-week HFD-fed mice. n = 3. Right: sorted Lin$^-$ (CD31$^-$/CD45$^-$) ASCs in EAT and IAT from 10-week HFD-fed mice. 2∼3 mice were pooled to each sample.
(J) mRNA levels of *Cxcl12* in EAT and IAT from 10-week HFD-fed mice. n = 6.
(K) Left: representative images of monocyte infiltration in the absence and presence of CXCL14 peptides. Right: quantification of monocyte migration. Scale bar, 100 μm.
(L) Monocyte migration in the absence and presence of CXCL14 and CXCL12 peptides. Negative control siRNA or *CXCR4* siRNA was treated with THP-1 monocytes before migration assay. Top: representative images of monocyte infiltration assay in the absence and presence of CXCL14 and CXCL12 peptides in CM from HFD-fed EAT and IAT. Bottom: quantification of monocyte migration. Red, cell tracker. Scale bar, 100 μm.
(M) Top: representative images of monocyte infiltration by *Cxcl14* siRNA in IAT ASCs. Bottom: quantification of monocyte migration. Scale bar, 100 μm.
(N) Top: representative images of monocyte infiltration assay by *Cxcl14* siRNA in EAT and IAT ASCs with CXCL12. Bottom: quantification of monocyte migration. Scale bar, 100 μm.
(O) Experimental scheme for *in vivo* monocyte migration assay.
(P) Quantification of *in vivo* monocyte migration with or without *Cxcl14* knockdown in IAT. n = 5. A connected line means data from the same mouse.
Data are represented as mean ± SD. Significance was determined using ANOVA (F, I, and K–N), Student's t test (I and J), or paired Student's t test (P). *p < 0.05, **p < 0.01, ***p < 0.001; n.s., non-significant.
See also Figure S4.

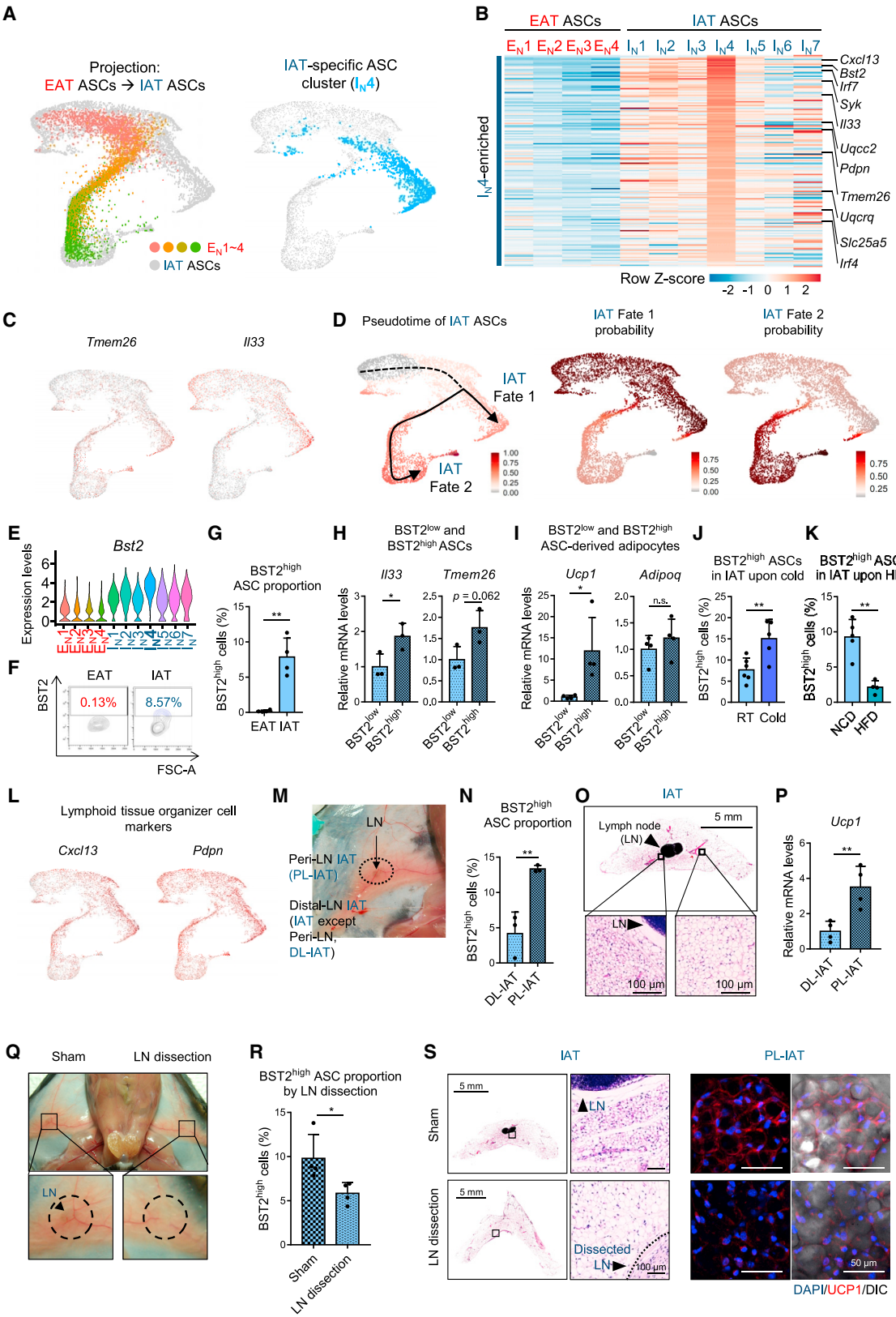

(legend on next page)

primarily determine their adipogenic potential. Second, at the onset of obesity, DPP4$^+$ ES1-specific proliferation stimulated by FGF and TGFβ signaling would induce EAT-selective *de novo* adipogenesis. Third, upon prolonged exposure to obesogenic stimuli, EAT-specific SDC1$^+$ ASCs would promote fibro-inflammatory remodeling, and IAT-specific CXCL14$^+$ ASCs would repress monocyte infiltration. Lastly, IAT-specific BST2^{high} ASCs appear to be pivotal in IAT-selective beige adipocyte biogenesis. Collectively, these data suggest that the distinct properties of ASC clusters from EAT and IAT would determine the fat depot-specific metabolic features.

ASC hierarchy is of importance to reveal the regulatory mechanisms of *de novo* adipogenesis in WAT. Although recent studies have revealed the ASC hierarchy in either EAT or IAT (Burl et al., 2018; Hepler et al., 2018; Merrick et al., 2019; Sárvári et al., 2021; Schwalie et al., 2018), comparative analysis of EAT and IAT ASC hierarchy and analysis of fat depot-specific regulatory mechanisms of ASC hierarchy have not been attempted. Our data showed that mouse EAT and IAT ASCs and their human counterparts can be largely categorized into three adipogenic stages. Nevertheless, gene expression profiles and cell populations in ASC clusters of each stage of EAT and IAT ASCs were strikingly different. ES1 ASCs consisted of about 15% of EAT ASCs, whereas IS1 ASCs were composed of more than 60% IAT ASCs, implying that regulatory mechanisms of ASC differentiation, including preadipocyte commitment, might differ between EAT and IAT ASCs. Transplantation experiments revealed that ES1 ASCs were innately prone to differentiation into ES2 and ES3 committed preadipocytes, whereas IS1 ASCs would be less likely to differentiate into IS2 and IS3 committed preadipocytes, probably due to intrinsic factors such as WNT signaling in IS1 ASCs. In line herewith, a genome-wide association study showed that SNPs in the *WNT2* promoter/enhancers are related to the waist-to-hip ratio in humans (Figure S2I). Together, these data suggest that the intrinsic features of ASC clusters in EAT and IAT would drive the fat depot-selective ASC hierarchy and *de novo* adipogenesis.

In the presence of chronic overnutrition, EAT and IAT undergo different remodeling processes, such as adipogenesis, fibrosis, and inflammation. In this study, we identified fat depot-specific ASCs responsible for the depot-specific remodeling processes. For example, DPP4$^+$ ES1 ASCs selectively proliferate, at least in part, through FGF and TGFβ signaling, leading to EAT-selective enhanced *de novo* adipogenesis in obesity. Consistent with this, it has been reported that *Fgf1* whole-body knockout mice exhibit dysregulated fat expansion in obesity (Jonker et al., 2012). Also, trajectory analysis indicated that EAT ASCs, not IAT ASCs, are fated to EAT-specific SDC1$^+$ fibro-inflammatory ASCs, a subpopulation of CD9$^+$ fibrogenic ASCs (Hepler et al., 2018; Marcelin et al., 2017), upon HFD. SDC1 has been reported to promote fibrosis by facilitating TGFβ signaling in the lungs (Parimon et al., 2019), implying that SDC1 would directly potentiate the fibrotic features of SDC1$^+$ ASCs. Moreover, we demonstrated that IAT-specific CXCL14$^+$ ASCs could mediate the anti-inflammatory effects in obese IAT by inhibiting the CXCL12-CXCR4 pathway in monocytes (Kim et al., 2014; Tanegashima et al., 2013), corroborating the recent findings that IAT ASCs could repress monocyte infiltration in obesity (Hwang et al., 2019). Thus, our analyses with lean and obese fat tissues have identified key ASC clusters that would be crucial for depot-selective adipose tissue remodeling in obesity.

Thermogenic beige adipocyte precursors would be distinct from white adipocyte precursors in IAT (Chen et al., 2019; Inagaki et al., 2016; Shapira and Seale, 2019; Sohn et al., 2018a; Wang and Seale, 2016; Wu et al., 2012; Yoneshiro et al., 2019). Here, our data show that IAT-specific BST2^{high} ASCs would serve as beige adipocyte precursors. IAT-specific BST2^{high} ASCs had distinct molecular profiles and progressed into different cell fates from other IAT ASCs. IAT-specific BST2^{high} ASCs highly expressed *Cxcl13*, *Il33*, and beige adipocyte precursor marker genes, including *Tmem26* (Wu et al., 2012). It is noteworthy that BST2^{high} ASCs were enriched near LNs, which are a distinct anatomical feature of IAT. Through LN dissection experiments, we showed that IAT LNs would potentiate BST2^{high} ASC biogenesis. It is plausible to speculate that IAT-specific BST2^{high} ASCs

Figure 5. In IAT, BST2^{high} ASCs are beige fat precursors whose biogenesis is regulated by lymph nodes

(A) Projection plot of EAT ASCs to IAT ASCs. EAT ASC clusters are projected to most similar IAT ASCs. IAT ASCs are shown in gray, and EAT ASC clusters are shown in color. I_N4 cluster marked by blue.
(B) Heatmap showing I_N4 cluster-specific genes.
(C) Expression levels of *Tmem26* and *Il33*.
(D) *In silico* pseudotime analysis and IAT Fate 1 and Fate 2 probabilistic analysis of IAT ASCs from NCD-fed mice.
(E) Expression levels of *Bst2* in ASCs.
(F and G) Representative FACS plots and proportion of BST2^{high} cells from ASCs in EAT and IAT. n = 4.
(H) mRNA levels of *Il33* and *Tmem26* in the sorted BST2^{high} and BST2^{low} ASCs. n = 3.
(I) mRNA levels of *Ucp1* and *Adipoq* in the differentiated BST2^{high} and BST2^{low} ASCs. n = 4.
(J) Proportion of BST2^{high} ASCs from mice at room temperature (RT) and upon cold exposure for 3 days. n = 5∼6.
(K) Proportion of BST2^{high} ASCs from NCD- and 8-week HFD-fed mice. n = 4.
(L) Expression levels of genes related to lymphoid tissue organizer cell markers *Cxcl13* and *Pdpn*.
(M) A representative macroscopic image of IAT. Lymph node (LN), peri-LN IAT (PL-IAT), and distal-LN IAT (DL-IAT) are represented. DL-IAT means IAT excluding the PL-IAT region.
(N) FACS analysis of BST2^{high} cells from DL-IAT and PL-IAT ASCs. n = 3.
(O and P) Representative histological images of adipose tissues and *Ucp1* expression from adult male mice at RT. n = 4. Scale bar, 5 mm or 100 μm.
(Q) A representative macroscopic image of IAT. IAT of sham operation and LN dissection were presented. An arrow indicates LN.
(R) FACS analysis of BST2^{high} cells from sham and LN dissection IAT. n = 4.
(S) Representative macroscopic images and whole-mount microscopic images of sham and LN dissection experiments 2 weeks after surgery at RT.
Data are represented as mean ± SD. Significance was determined using Student's t test. *p < 0.05, **p < 0.01.
See also Figure S5.

might recruit immune cells such as type 2 innate lymphoid cells through IL33 secretion, which is important for beige fat formation (Brestoff et al., 2015; Rajbhandari et al., 2019; Rajbhandari et al., 2018; Villarroya et al., 2018). In accordance with this, human thermogenic beige adipocytes are abundant in the neck and supraclavicular regions, which are rich in LNs (Cypess et al., 2009). Further, human LNs are abundant in VAT, but rare in SAT (Redondo et al., 2020). Thus, human LNs near fat depots might also contribute to beige adipocyte biogenesis upon cold exposure. Together, these data propose that IAT-specific BST2^{high} ASCs would be important for the formation of IAT-specific thermogenic adipocytes and that IAT LNs would be involved in thermogenesis through enrichment of IAT-specific BST2^{high} beige precursors. Nonetheless, further studies are needed to elucidate the detailed mechanism(s) by which LNs could affect BST2^{high} ASCs in IAT.

In conclusion, we examined and scrutinized heterogeneous ASCs in two white fat depots and elucidated specific ASC clusters that contribute to fat depot-selective features. Our data indicate that the distinct characteristics of fat depot-specific ASC subpopulations are critical for the different pathophysiological features of EAT and IAT upon metabolic stimuli. Taken together, our comprehensive ASC map provided by this study broadens our understanding of ASC heterogeneity, which is pivotal for the different features of EAT and IAT in the regulation of systemic metabolism.

Limitations of study

The primary goal of this study was to identify and characterize fat depot-specific ASC clusters through comparative analyses. Although we extensively explored ASC clusters and molecular properties of the key ASC clusters that modulate fat depot-specific features, such as *de novo* adipogenesis, fibrosis, inflammatory responses, and thermogenesis, exclusive investigations of these ASC clusters through selective removal of ASC clusters or genetic manipulation of key genes in each ASC cluster were not performed. In addition, as our dataset did not include the adipocyte fraction and SVFs other than ASCs, the effects of distinct ASC clusters in EAT and IAT on the different features of EAT and IAT adipocytes were not thoroughly covered. In addition, we cannot exclude the possibility that surgical interventions such as LN dissection might damage sympathetic nerves in PL-IAT. Lastly, investigations in genetically modified animal models will be informative to uncover the pathophysiological significance of each ASC cluster in systemic energy homeostasis.

STAR★METHODS

Detailed methods are provided in the online version of this paper and include the following:

SUPPLEMENTAL INFORMATION

Supplemental information can be found online at https://doi.org/10.1016/j.cmet.2021.11.014.

ACKNOWLEDGMENTS

We are grateful to Hye Jin Noh for helping with the FACS experiments. This study was supported by the National Research Foundation, funded by the Korean government (Ministry of Science and ICT; 2017M3A9B6073099 and 2020R1A2C400163011 to J.K.K. and NRF-2018R1A5A1024340 and NRF-2020R1A3B2078617 to J.B.K.). H.N., Y.G.J., S.M.H., J.P., Y.J., J.H.S., J.S.H., and Y.Y.K. were supported by the BK21 Plus program.

AUTHOR CONTRIBUTIONS

H.N. and Y.G.J. conceptualized the study, performed the experiments, analyzed the data, and wrote the manuscript. E.S.P. and Y.H.C. analyzed the scRNA-seq data. S.M.H., J.P., J.H.S., J.S.H., Y.Y.K., and I.H. performed the animal experiments. Y.J. performed microscopic experiments. Y.K.L., T.J.O., and S.H.C. performed the experiments on human adipose tissue. J.Y.H. and S.S.C. discussed the study and contributed to the writing of the manuscript. J.K.K. curated and analyzed the scRNA-seq data and wrote the manuscript. J.B.K. supervised the study and wrote the manuscript.

DECLARATION OF INTERESTS

The authors declare no competing financial interests.

Received: March 23, 2021
Revised: September 16, 2021
Accepted: November 22, 2021
Published: January 11, 2022

REFERENCES

Angueira, A.R., Sakers, A.P., Holman, C.D., Cheng, L., Arbocco, M.N., Shamsi, F., Lynes, M.D., Shrestha, R., Okada, C., Batmanov, K., et al. (2021). Defining the lineage of thermogenic perivascular adipose tissue. Nat. Metab. *3*, 469–484.

Bénézech, C., Mader, E., Desanti, G., Khan, M., Nakamura, K., White, A., Ware, C.F., Anderson, G., and Caamaño, J.H. (2012). Lymphotoxin-β receptor signaling through NF-κB2-RelB pathway reprograms adipocyte precursors as lymph node stromal cells. Immunity *37*, 721–734.

Berry, R., and Rodeheffer, M.S. (2013). Characterization of the adipocyte cellular lineage in vivo. Nat. Cell Biol. *15*, 302–308.

Boyle, K.B., Hadaschik, D., Virtue, S., Cawthorn, W.P., Ridley, S.H., O'Rahilly, S., and Siddle, K. (2009). The transcription factors Egr1 and Egr2 have

opposing influences on adipocyte differentiation. Cell Death Differ. *16*, 782–789.

Brestoff, J.R., Kim, B.S., Saenz, S.A., Stine, R.R., Monticelli, L.A., Sonnenberg, G.F., Thome, J.J., Farber, D.L., Lutfy, K., Seale, P., and Artis, D. (2015). Group 2 innate lymphoid cells promote beiging of white adipose tissue and limit obesity. Nature *519*, 242–246.

Burl, R.B., Ramseyer, V.D., Rondini, E.A., Pique-Regi, R., Lee, Y.H., and Granneman, J.G. (2018). Deconstructing adipogenesis induced by β3-adrenergic receptor activation with single-cell expression profiling. Cell Metab. *28*, 300–309.e4.

Chen, Y., Ikeda, K., Yoneshiro, T., Scaramozza, A., Tajima, K., Wang, Q., Kim, K., Shinoda, K., Sponton, C.H., Brown, Z., et al. (2019). Thermal stress induces glycolytic beige fat formation via a myogenic state. Nature *565*, 180–185.

Choe, S.S., Huh, J.Y., Hwang, I.J., Kim, J.I., and Kim, J.B. (2016). Adipose tissue remodeling: its role in energy metabolism and metabolic disorders. Front. Endocrinol. (Lausanne) *7*, 30.

Choi, Y.H., and Kim, J.K. (2019). Dissecting cellular heterogeneity using single-cell RNA sequencing. Mol. Cells *42*, 189–199.

Chouchani, E.T., and Kajimura, S. (2019). Metabolic adaptation and maladaptation in adipose tissue. Nat Metab *1*, 189–200.

Christodoulides, C., Lagathu, C., Sethi, J.K., and Vidal-Puig, A. (2009). Adipogenesis and WNT signalling. Trends Endocrinol. Metab. *20*, 16–24.

Cristancho, A.G., and Lazar, M.A. (2011). Forming functional fat: a growing understanding of adipocyte differentiation. Nat. Rev. Mol. Cell Biol. *12*, 722–734.

Cypess, A.M., Lehman, S., Williams, G., Tal, I., Rodman, D., Goldfine, A.B., Kuo, F.C., Palmer, E.L., Tseng, Y.H., Doria, A., et al. (2009). Identification and importance of brown adipose tissue in adult humans. N. Engl. J. Med. *360*, 1509–1517.

Ferrero, R., Rainer, P., and Deplancke, B. (2020). Toward a consensus view of mammalian adipocyte stem and progenitor cell heterogeneity. Trends Cell Biol. *30*, 937–950.

Gesta, S., Tseng, Y.H., and Kahn, C.R. (2007). Developmental origin of fat: tracking obesity to its source. Cell *131*, 242–256.

Gu, W., Nowak, W.N., Xie, Y., Le Bras, A., Hu, Y., Deng, J., Issa Bhaloo, S., Lu, Y., Yuan, H., Fidanis, E., et al. (2019). Single-cell RNA-sequencing and metabolomics analyses reveal the contribution of perivascular adipose tissue stem cells to vascular remodeling. Arterioscler. Thromb. Vasc. Biol. *39*, 2049–2066.

Han, J.S., Lee, J.H., Kong, J., Ji, Y., Kim, J., Choe, S.S., and Kim, J.B. (2019). Hypoxia restrains lipid utilization via protein kinase A and adipose triglyceride lipase downregulation through hypoxia-inducible factor. Mol. Cell. Biol. *39*, e00390–e00318.

Hepler, C., Shan, B., Zhang, Q., Henry, G.H., Shao, M., Vishvanath, L., Ghaben, A.L., Mobley, A.B., Strand, D., Hon, G.C., and Gupta, R.K. (2018). Identification of functionally distinct fibro-inflammatory and adipogenic stromal subpopulations in visceral adipose tissue of adult mice. eLife *7*, e39636.

Hill, D.A., Lim, H.W., Kim, Y.H., Ho, W.Y., Foong, Y.H., Nelson, V.L., Nguyen, H.C.B., Chegireddy, K., Kim, J., Habertheuer, A., et al. (2018). Distinct macrophage populations direct inflammatory versus physiological changes in adipose tissue. Proc. Natl. Acad. Sci. USA *115*, E5096–E5105.

Hu, L., Yang, G., Hägg, D., Sun, G., Ahn, J.M., Jiang, N., Ricupero, C.L., Wu, J., Rodhe, C.H., Ascherman, J.A., et al. (2015). IGF1 promotes adipogenesis by a lineage bias of endogenous adipose stem/progenitor cells. Stem Cells *33*, 2483–2495.

Hu, W., Jiang, C., Guan, D., Dierickx, P., Zhang, R., Moscati, A., Nadkarni, G.N., Steger, D.J., Loos, R.J.F., Hu, C., et al. (2019). Patient adipose stem cell-derived adipocytes reveal genetic variation that predicts antidiabetic drug response. Cell Stem Cell *24*, 299–308.e6.

Hwang, I., and Kim, J.B. (2019). Two faces of white adipose tissue with heterogeneous adipogenic progenitors. Diabetes Metab. J. *43*, 752–762.

Hwang, I., Jo, K., Shin, K.C., Kim, J.I., Ji, Y., Park, Y.J., Park, J., Jeon, Y.G., Ka, S., Suk, S., et al. (2019). GABA-stimulated adipose-derived stem cells suppress subcutaneous adipose inflammation in obesity. Proc. Natl. Acad. Sci. USA *116*, 11936–11945.

Inagaki, T., Sakai, J., and Kajimura, S. (2016). Transcriptional and epigenetic control of brown and beige adipose cell fate and function. Nat. Rev. Mol. Cell Biol. *17*, 480–495.

Jeffery, E., Church, C.D., Holtrup, B., Colman, L., and Rodeheffer, M.S. (2015). Rapid depot-specific activation of adipocyte precursor cells at the onset of obesity. Nat. Cell Biol. *17*, 376–385.

Jeffery, E., Wing, A., Holtrup, B., Sebo, Z., Kaplan, J.L., Saavedra-Peña, R., Church, C.D., Colman, L., Berry, R., and Rodeheffer, M.S. (2016). The adipose tissue microenvironment regulates depot-specific adipogenesis in obesity. Cell Metab. *24*, 142–150.

Jeon, Y.G., Lee, J.H., Ji, Y., Sohn, J.H., Lee, D., Kim, D.W., Yoon, S.G., Shin, K.C., Park, J., Seong, J.K., et al. (2020). RNF20 functions as a transcriptional coactivator for PPARγ by promoting NCoR1 degradation in adipocytes. Diabetes *69*, 20–34.

Jonker, J.W., Suh, J.M., Atkins, A.R., Ahmadian, M., Li, P., Whyte, J., He, M., Juguilon, H., Yin, Y.Q., Phillips, C.T., et al. (2012). A PPARγ-FGF1 axis is required for adaptive adipose remodelling and metabolic homeostasis. Nature *485*, 391–394.

Kim, D., Kim, J., Yoon, J.H., Ghim, J., Yea, K., Song, P., Park, S., Lee, A., Hong, C.P., Jang, M.S., et al. (2014). CXCL12 secreted from adipose tissue recruits macrophages and induces insulin resistance in mice. Diabetologia *57*, 1456–1465.

Kim, J.I., Huh, J.Y., Sohn, J.H., Choe, S.S., Lee, Y.S., Lim, C.Y., Jo, A., Park, S.B., Han, W., and Kim, J.B. (2015). Lipid-overloaded enlarged adipocytes provoke insulin resistance independent of inflammation. Mol. Cell. Biol. *35*, 1686–1699.

Kolodziejczyk, A.A., Kim, J.K., Svensson, V., Marioni, J.C., and Teichmann, S.A. (2015). The technology and biology of single-cell RNA sequencing. Mol. Cell *58*, 610–620.

Kong, J., Ji, Y., Jeon, Y.G., Han, J.S., Han, K.H., Lee, J.H., Lee, G., Jang, H., Choe, S.S., Baes, M., and Kim, J.B. (2020). Spatiotemporal contact between peroxisomes and lipid droplets regulates fasting-induced lipolysis via PEX5. Nat. Commun. *11*, 578.

Korsunsky, I., Millard, N., Fan, J., Slowikowski, K., Zhang, F., Wei, K., Baglaenko, Y., Brenner, M., Loh, P.R., and Raychaudhuri, S. (2019). Fast, sensitive and accurate integration of single-cell data with Harmony. Nat. Methods *16*, 1289–1296.

Lee, Y.S., and Olefsky, J. (2021). Chronic tissue inflammation and metabolic disease. Genes Dev. *35*, 307–328.

Lee, J.H., Jeon, Y.G., Lee, K.H., Lee, H.W., Park, J., Jang, H., Kang, M., Lee, H.S., Cho, H.J., Nam, D.H., et al. (2017). RNF20 suppresses tumorigenesis by inhibiting the SREBP1c-PTTG1 axis in kidney cancer. Mol. Cell. Biol. *37*, e00265–e00217.

Lee, Y.K., Sohn, J.H., Han, J.S., Park, Y.J., Jeon, Y.G., Ji, Y., Dalen, K.T., Sztalryd, C., Kimmel, A.R., and Kim, J.B. (2018). *Perilipin 3* deficiency stimulates thermogenic beige adipocytes through *PPARα* activation. Diabetes *67*, 791–804.

Lun, A.T., McCarthy, D.J., and Marioni, J.C. (2016). A step-by-step workflow for low-level analysis of single-cell RNA-seq data with Bioconductor. F1000Res. *5*, 2122.

Lun, A.T.L., Riesenfeld, S., Andrews, T., Dao, T.P., Gomes, T., and Marioni, J.C.; participants in the 1st Human Cell Atlas Jamboree (2019). EmptyDrops: distinguishing cells from empty droplets in droplet-based single-cell RNA sequencing data. Genome Biol. *20*, 63.

Macotela, Y., Emanuelli, B., Mori, M.A., Gesta, S., Schulz, T.J., Tseng, Y.H., and Kahn, C.R. (2012). Intrinsic differences in adipocyte precursor cells from different white fat depots. Diabetes *61*, 1691–1699.

Marcelin, G., Ferreira, A., Liu, Y., Atlan, M., Aron-Wisnewsky, J., Pelloux, V., Botbol, Y., Ambrosini, M., Fradet, M., Rouault, C., et al. (2017). A PDGFRα-mediated switch toward $CD9^{high}$ adipocyte progenitors controls obesity-induced adipose tissue fibrosis. Cell Metab. *25*, 673–685.

McCarthy, D.J., Campbell, K.R., Lun, A.T., and Wills, Q.F. (2017). Scater: pre-processing, quality control, normalization and visualization of single-cell RNA-seq data in R. Bioinformatics *33*, 1179–1186.

Merrick, D., Sakers, A., Irgebay, Z., Okada, C., Calvert, C., Morley, M.P., Percec, I., and Seale, P. (2019). Identification of a mesenchymal progenitor cell hierarchy in adipose tissue. Science *364*, eaav2501.

Nguyen, T.T.P., Kim, D.Y., Lee, Y.G., Lee, Y.S., Truong, X.T., Lee, J.H., Song, D.K., Kwon, T.K., Park, S.H., Jung, C.H., et al. (2021). SREBP-1c impairs ULK1 sulfhydration-mediated autophagic flux to promote hepatic steatosis in high-fat-diet-fed mice. Mol. Cell *81*, 3820–3832.e7.

Oguri, Y., Shinoda, K., Kim, H., Alba, D.L., Bolus, W.R., Wang, Q., Brown, Z., Pradhan, R.N., Tajima, K., Yoneshiro, T., et al. (2020). CD81 controls beige fat progenitor cell growth and energy balance via FAK signaling. Cell *182*, 563–577.e20.

Parimon, T., Yao, C., Habiel, D.M., Ge, L., Bora, S.A., Brauer, R., Evans, C.M., Xie, T., Alonso-Valenteen, F., Medina-Kauwe, L.K., et al. (2019). Syndecan-1 promotes lung fibrosis by regulating epithelial reprogramming through extracellular vesicles. JCI Insight *5*, e129359.

Park, J., Huh, J.Y., Oh, J., Kim, J.I., Han, S.M., Shin, K.C., Jeon, Y.G., Choe, S.S., Park, J., and Kim, J.B. (2019). Activation of invariant natural killer T cells stimulates adipose tissue remodeling via adipocyte death and birth in obesity. Genes Dev. *33*, 1657–1672.

Pischon, T., Boeing, H., Hoffmann, K., Bergmann, M., Schulze, M.B., Overvad, K., van der Schouw, Y.T., Spencer, E., Moons, K.G., Tjønneland, A., et al. (2008). General and abdominal adiposity and risk of death in Europe. N. Engl. J. Med. *359*, 2105–2120.

Qiu, X., Mao, Q., Tang, Y., Wang, L., Chawla, R., Pliner, H.A., and Trapnell, C. (2017). Reversed graph embedding resolves complex single-cell trajectories. Nat. Methods *14*, 979–982.

Rajbhandari, P., Thomas, B.J., Feng, A.C., Hong, C., Wang, J., Vergnes, L., Sallam, T., Wang, B., Sandhu, J., Seldin, M.M., et al. (2018). IL-10 signaling remodels adipose chromatin architecture to limit thermogenesis and energy expenditure. Cell *172*, 218–233.e17.

Rajbhandari, P., Arneson, D., Hart, S.K., Ahn, I.S., Diamante, G., Santos, L.C., Zaghari, N., Feng, A.C., Thomas, B.J., Vergnes, L., et al. (2019). Single cell analysis reveals immune cell-adipocyte crosstalk regulating the transcription of thermogenic adipocytes. eLife *8*, e49501.

Redondo, P.A.G., Gubert, F., Zaverucha-do-Valle, C., Dutra, T.P.P., Ayres-Silva, J.P., Fernandes, N., de Souza, A.A.P., Loizidou, M., Takiya, C.M., Rossi, M.I.D., and Borojevic, R. (2020). Lymphatic vessels in human adipose tissue. Cell Tissue Res. *379*, 511–520.

Reilly, S.M., and Saltiel, A.R. (2017). Adapting to obesity with adipose tissue inflammation. Nat. Rev. Endocrinol. *13*, 633–643.

Rodeheffer, M.S., Birsoy, K., and Friedman, J.M. (2008). Identification of white adipocyte progenitor cells in vivo. Cell *135*, 240–249.

Rosen, E.D., and Spiegelman, B.M. (2014). What we talk about when we talk about fat. Cell *156*, 20–44.

Ross, S.E., Hemati, N., Longo, K.A., Bennett, C.N., Lucas, P.C., Erickson, R.L., and MacDougald, O.A. (2000). Inhibition of adipogenesis by Wnt signaling. Science *289*, 950–953.

Saltiel, A.R., and Olefsky, J.M. (2017). Inflammatory mechanisms linking obesity and metabolic disease. J. Clin. Invest. *127*, 1–4.

Sanchez-Gurmaches, J., Hung, C.M., and Guertin, D.A. (2016). Emerging complexities in adipocyte origins and identity. Trends Cell Biol. *26*, 313–326.

Sárvári, A.K., Van Hauwaert, E.L., Markussen, L.K., Gammelmark, E., Marcher, A.B., Ebbesen, M.F., Nielsen, R., Brewer, J.R., Madsen, J.G.S., and Mandrup, S. (2021). Plasticity of epididymal adipose tissue in response to diet-induced obesity at single-nucleus resolution. Cell Metab. *33*, 437–453.e5.

Schubert, M., Klinger, B., Klünemann, M., Sieber, A., Uhlitz, F., Sauer, S., Garnett, M.J., Blüthgen, N., and Saez-Rodriguez, J. (2018). Perturbation-response genes reveal signaling footprints in cancer gene expression. Nat. Commun. *9*, 20.

Schwalie, P.C., Dong, H., Zachara, M., Russeil, J., Alpern, D., Akchiche, N., Caprara, C., Sun, W., Schlaudraff, K.U., Soldati, G., et al. (2018). A stromal cell population that inhibits adipogenesis in mammalian fat depots. Nature *559*, 103–108.

Setty, M., Kiseliovas, V., Levine, J., Gayoso, A., Mazutis, L., and Pe'er, D. (2019). Characterization of cell fate probabilities in single-cell data with Palantir. Nat. Biotechnol. *37*, 451–460.

Shamsi, F., Piper, M., Ho, L.L., Huang, T.L., Gupta, A., Streets, A., Lynes, M.D., and Tseng, Y.H. (2021). Vascular smooth muscle-derived Trpv1^{+} progenitors are a source of cold-induced thermogenic adipocytes. Nat. Metab. *3*, 485–495.

Shapira, S.N., and Seale, P. (2019). Transcriptional control of brown and beige fat development and function. Obesity (Silver Spring) *27*, 13–21.

Shungin, D., Winkler, T.W., Croteau-Chonka, D.C., Ferreira, T., Locke, A.E., Mägi, R., Strawbridge, R.J., Pers, T.H., Fischer, K., Justice, A.E., et al.; ADIPOGen Consortium; CARDIOGRAMplusC4D Consortium; CKDGen Consortium; GEFOS Consortium; GENIE Consortium; GLGC; ICBP; International Endogene Consortium; LifeLines Cohort Study; MAGIC Investigators; MuTHER Consortium; PAGE Consortium; ReproGen Consortium (2015). New genetic loci link adipose and insulin biology to body fat distribution. Nature *518*, 187–196.

Sillat, T., Saat, R., Pöllänen, R., Hukkanen, M., Takagi, M., and Konttinen, Y.T. (2012). Basement membrane collagen type IV expression by human mesenchymal stem cells during adipogenic differentiation. J. Cell. Mol. Med. *16*, 1485–1495.

Sohn, J.H., Kim, J.I., Jeon, Y.G., Park, J., and Kim, J.B. (2018a). Effects of three thiazolidinediones on metabolic regulation and cold-induced thermogenesis. Mol. Cells *41*, 900–908.

Sohn, J.H., Lee, Y.K., Han, J.S., Jeon, Y.G., Kim, J.I., Choe, S.S., Kim, S.J., Yoo, H.J., and Kim, J.B. (2018b). Perilipin 1 (Plin1) deficiency promotes inflammatory responses in lean adipose tissue through lipid dysregulation. J. Biol. Chem. *293*, 13974–13988.

Stuart, T., Butler, A., Hoffman, P., Hafemeister, C., Papalexi, E., Mauck, W.M., 3rd, Hao, Y., Stoeckius, M., Smibert, P., and Satija, R. (2019). Comprehensive integration of single-cell data. Cell *177*, 1888–1902.e21.

Sun, K., Kusminski, C.M., and Scherer, P.E. (2011). Adipose tissue remodeling and obesity. J. Clin. Invest. *121*, 2094–2101.

Tabula Muris Consortium; Overall coordination; Logistical coordination; Organ collection and processing; Library preparation and sequencing; Computational data analysis; Cell type annotation; Writing group; Supplemental text writing group; Principal investigators (2018). Single-cell transcriptomics of 20 mouse organs creates a Tabula Muris. Nature *562*, 367–372.

Tanegashima, K., Suzuki, K., Nakayama, Y., Tsuji, K., Shigenaga, A., Otaka, A., and Hara, T. (2013). CXCL14 is a natural inhibitor of the CXCL12-CXCR4 signaling axis. FEBS Lett. *587*, 1731–1735.

Tang, W., Zeve, D., Suh, J.M., Bosnakovski, D., Kyba, M., Hammer, R.E., Tallquist, M.D., and Graff, J.M. (2008). White fat progenitor cells reside in the adipose vasculature. Science *322*, 583–586.

Tchkonia, T., Thomou, T., Zhu, Y., Karagiannides, I., Pothoulakis, C., Jensen, M.D., and Kirkland, J.L. (2013). Mechanisms and metabolic implications of regional differences among fat depots. Cell Metab. *17*, 644–656.

van de Pavert, S.A., Olivier, B.J., Goverse, G., Vondenhoff, M.F., Greuter, M., Beke, P., Kusser, K., Höpken, U.E., Lipp, M., Niederreither, K., et al. (2009). Chemokine CXCL13 is essential for lymph node initiation and is induced by retinoic acid and neuronal stimulation. Nat. Immunol. *10*, 1193–1199.

Vijay, J., Gauthier, M.F., Biswell, R.L., Louiselle, D.A., Johnston, J.J., Cheung, W.A., Belden, B., Pramatarova, A., Biertho, L., Gibson, M., et al. (2020). Single-cell analysis of human adipose tissue identifies depot and disease specific cell types. Nat. Metab. *2*, 97–109.

Villanueva, C.J., Waki, H., Godio, C., Nielsen, R., Chou, W.L., Vargas, L., Wroblewski, K., Schmedt, C., Chao, L.C., Boyadjian, R., et al. (2011). TLE3 is a dual-function transcriptional coregulator of adipogenesis. Cell Metab. *13*, 413–427.

Villarroya, F., Cereijo, R., Villarroya, J., Gavaldà-Navarro, A., and Giralt, M. (2018). Toward an understanding of how immune cells control brown and beige adipobiology. Cell Metab. *27*, 954–961.

Wang, W., and Seale, P. (2016). Control of brown and beige fat development. Nat. Rev. Mol. Cell Biol. *17*, 691–702.

Wang, Q.A., Tao, C., Gupta, R.K., and Scherer, P.E. (2013). Tracking adipogenesis during white adipose tissue development, expansion and regeneration. Nat. Med. *19*, 1338–1344.

Wang, W., Ishibashi, J., Trefely, S., Shao, M., Cowan, A.J., Sakers, A., Lim, H.W., O'Connor, S., Doan, M.T., Cohen, P., et al. (2019). A PRDM16-driven metabolic signal from adipocytes regulates precursor cell fate. Cell Metab. *30*, 174–189.e5.

Wu, J., Boström, P., Sparks, L.M., Ye, L., Choi, J.H., Giang, A.H., Khandekar, M., Virtanen, K.A., Nuutila, P., Schaart, G., et al. (2012). Beige adipocytes are a distinct type of thermogenic fat cell in mouse and human. Cell *150*, 366–376.

Yoneshiro, T., Wang, Q., Tajima, K., Matsushita, M., Maki, H., Igarashi, K., Dai, Z., White, P.J., McGarrah, R.W., Ilkayeva, O.R., et al. (2019). BCAA catabolism in brown fat controls energy homeostasis through SLC25A44. Nature *572*, 614–619.

Zuriaga, M.A., Fuster, J.J., Gokce, N., and Walsh, K. (2017). Humans and mice display opposing patterns of "browning" gene expression in visceral and subcutaneous white adipose tissue depots. Front. Cardiovasc. Med. *4*, 27.

STAR★METHODS

KEY RESOURCES TABLE

REAGENT or RESOURCE	SOURCE	IDENTIFIER
Antibodies		
Alexa Fluor 647 anti-Tyrosine Hydroxylase Antibody	BioLegend	Cat# 818007; RRID: AB_2801154
APC anti-human CD31 Antibody	BioLegend	Cat# 303115; RRID: AB_1877152
APC anti-human CD45 Antibody	BioLegend	Cat# 304011; RRID: AB_314399
APC anti-mouse CD31 Antibody	BioLegend	Cat# 102409; RRID: AB_312904
APC anti-mouse CD317 (BST2, PDCA-1) Antibody	BioLegend	Cat# 127015; RRID: AB_1967101
APC anti-mouse CD45 Antibody	BioLegend	Cat# 103111; RRID: AB_312976
APC anti-mouse CD9 Antibody	BioLegend	Cat# 124811; RRID: AB_2783070
APC/Cyanine7 anti-mouse/human CD11b Antibody	BioLegend	Cat# 101225; RRID: AB_830641
F4/80 Monoclonal Antibody (BM8), PerCP-Cyanine5.5	eBioscience	Cat# 45-4801-82; RRID: AB_914345
FITC anti-human CD45 Antibody	BioLegend	Cat# 304005; RRID: AB_314393
FITC anti-mouse CD31 Antibody	BioLegend	Cat# 102405; RRID: AB_312900
FITC anti-mouse CD45 Antibody	BioLegend	Cat# 103107; RRID: AB_312972
FITC anti-mouse/human Ki-67 Antibody	BioLegend	Cat# 151211; RRID: AB_2814054
FITC Rat Anti-Mouse CD31 Antibody	BD Biosciences	Cat# 558738; RRID: AB_397097
PE anti-human CD54 (ICAM1) Antibody	BioLegend	Cat# 353105; RRID: AB_10899575
PE anti-mouse CD54 (ICAM1) Antibody	BioLegend	Cat# 116107; RRID: AB_313698
PE anti-mouse SDC1 (CD138) Antibody	Thermo Fisher	Cat# MA5-23527; RRID: AB_2609280
PE/Cy7 anti-mouse CD26 (DPP4) Antibody	BioLegend	Cat# 137809; RRID: AB_2564311
PE/Cyanine7 anti-human CD26 (DPP4) Antibody	BioLegend	Cat# 302713; RRID: AB_2563992
PerCP-Cy5.5 anti-mouse CD31 Antibody	BioLegend	Cat# 102419; RRID: AB_10612742
PerCP-Cy5.5 anti-mouse CD45 Antibody	BioLegend	Cat# 103131; RRID: AB_893344
PerCP-eFluor 710, Ki-67 Monoclonal Antibody (SolA15)	eBiosciences	Cat# 46-5698-82; RRID: AB_11040981
UCP1 anti-rabbit Antibody	Cell Signaling	Cat# 14670; RRID: AB_2687530
Biological samples		
Human adipose tissues	This paper	N/A
Chemicals, peptides, and recombinant proteins		
3,3′,5-Triiodo-L-thyronine	Sigma-Aldrich	Cat# T2877
7-AAD	BD Biosciences	Cat# 51-2359KC
BAY 11-7082	Cayman Chemical	Cat# 10010266
BODIPY	Thermo Fisher	Cat# D3922
Bovine serum albumin, FFA-free	GenDEPOT	Cat# A0100-010
CCK-8 assay kit	Dojindo	Cat# CK04-11
CellTracker-Red CMTPX	Thermo Fisher	Cat# C34552
Chromium i7 Multiplex Kit	10X Genomics	Cat# PN-120262
Chromium Single Cell 3′ Library & Gel Bead Kit	10X Genomics	Cat# PN-1000092
Chromium Single Cell 30 Library & Gel Bead Kit v2	10X Genomics	Cat# PN-120267
Chromium Single Cell B Chip kit	10X Genomics	Cat# PN-1000074
CL 316,243 hydrate	Sigma-Aldrich	Cat# C5977
Collagenase type I	Worthington	Cat# 49A18993
CXCL12 peptide	R&D systems	Cat# 460-SD.
CXCL14 peptide	R&D systems	Cat# 730-XC
Dexamethasone	Sigma-Aldrich	Cat# D1756
Direct-zol RNA MiniPrep	Zymo Research	Cat# R2062

(*Continued on next page*)

Continued

REAGENT or RESOURCE	SOURCE	IDENTIFIER
DMEM, high glucose	Welgene	Cat# LM001-05
DMEM/F12	Sigma-Aldrich	Cat# D6421-500ML
Fetal bovine serum	Young In Frontier	Cat# US-FBS-500
FITC BrdU flow kit	BD Biosciences	Cat# 559619
Greiner Leucosep tube	Sigma-Aldrich	Cat# GN163290
Hoechst 33342	Thermo Fisher	Cat# 62249
IC261	Selleckchem	Cat# S8237
In vivo-jetPEI	Polyplus-Transfection	Cat# 201-50G
Indomethacin	Sigma-Aldrich	Cat# I8280
Insulin	Sigma-Aldrich	Cat# I5500
Isobutylmethylxanthine	Acros organics	Cat# 228420010
Matrigel	Corning	Cat# 356230
NU7441 (KU-57788)	Selleckchem	Cat# S2638
NycoPrep 1.077	Axis-Shield PoCAS	Cat# 1114550
PD-98059	Enzo Life Sciences	Cat# BML-EI360-0005
qRT-PCR 2X mix	BioFact	Cat# DQ384-40 h
Deposited data		
Bulk RNA-seq data	This paper	GEO: GSE168906
Bulk RNA-seq data	(Hwang et al., 2019)	GEO: GSE129665
GTEx dataset v7	GTEx	http://www.gtexportal.org/home
Microarray data	(Kim et al., 2015)	GEO: GSE65557
Single-cell RNA-seq dataset	This paper	BioProject: PRJNA708350
Single-cell RNA-seq dataset	(Burl et al., 2018)	SRA: SRP145475
Single-cell RNA-seq dataset	(Vijay et al., 2020)	GEO: GSE136230
Tabula Muris	(Tabula Muris Consortium et al., 2018)	https://tabula-muris.ds.czbiohub.org
Type 2 diabetes genetics dataset	Type 2 diabetes genetics	http://www.type2diabetesgenetics.org
Experimental models: Organisms/strains		
C57BL/6 mice	Central Lab Animal Inc	N/A
GFP-Tg mice	The Jackson Laboratory	Cat# 003291
Oligonucleotides		
For a full list of qRT-PCR primers, see Table S1	This paper	N/A
Software and algorithms		
DropletUtils	(Lun et al., 2019)	N/A
FlowJo software Version 10.5.3	BD	https://www.flowjo.com/
GraphPad Prism	GraphPad	https://www.graphpad.com/
Harmonypy	(Korsunsky et al., 2019)	N/A
Monocle2	(Qiu et al., 2017)	N/A
Palantir	(Setty et al., 2019)	N/A
Progeny	(Schubert et al., 2018)	N/A
R	R Development Core Team	https://cran.r-project.org
Scater	(McCarthy et al., 2017)	N/A
Scran	(Lun et al., 2016)	N/A
Seurat	(Stuart et al., 2019)	N/A
TopGO	N/A	https://doi.org/10.18129/B9.bioc.topGO
Other		
High-fat diet	Research Diets	Cat# D12492

RESOURCE AVAILABILITY

Lead Contact

Further information and requests for resources and reagents should be directed to and will be fulfilled by the lead contact, Jae Bum Kim (jaebkim@snu.ac.kr).

Materials Availability

This study did not generate new unique reagents.

Data and Code Availability

- Single-cell RNA-seq data have been deposited at GEO and are publicly available as of the date of publication. Accession numbers are listed in the key resources table.
- All original code has been depositied at https://github.com/scg-dgist/CELL-METABOLISM-adipose-stem-cell.
- Any additional information required to reanalyze the data reported in this paper is available from the lead contact upon request.

EXPERIMENTAL MODEL AND SUBJECT DETAILS

Animals

Eight-to-ten-week-old C57BL/6 mice were purchased from Central Lab Animal Incorporation (Seoul, Korea). C57BL/6 background GFP^+ transgenic (Tg) mice were generously gifted by Gou Young Koh (KAIST, Daejeon, South Korea). The mice were housed in a specific pathogen-free, temperature- and humidity-controlled animal facility at 22°C under a 12-h/12-h light/dark cycle. The mice were used directly after importing into the facility and their health status was checked 3 times a week during the experiment. High-fat diet feeding experiments were performed using 8-week-old mice fed a diet consisting of 60% calories from fat (D12492, Research Diets). BrdU (559619, BD Biosciences) was administered in the drinking water at 0.8 mg/mL for one week. For *in vivo Cxcl14* suppression, NCD- and 10-week HFD-fed mice received a dose of 20 μg/single IAT pad of control siRNA (siNC) or si*Cxcl14* complexed with *in vivo*-jetPEI (Polyplus Transfection, Cat# 201-50G) every 3 days for 2 weeks (Nguyen et al., 2021). Control siRNA was injected into IAT in the left flanks and si*Cxcl14* was injected into IAT in the right flanks. 2 weeks after siRNA injection, GFP^+ blood mononuclear cells were intravenously injected into mice and sacrificed on the following day. The animal study was approved by the Institutional Animal Care and Use Committee of the Seoul National University.

Human Subjects

Human adipose tissue samples were obtained during weight reduction laparoscopic bypass surgery at the Metabolic Surgery Center in Seoul National University Bundang Hospital (SNUBH). This study was conducted in accordance with the Declaration of Helsinki and was approved by the Ethics Committee of the SNUBH (IRB No. B-1801445301 & B-1812513302). All subjects agreed to provide their written informed consent. All subjects were female, aged 30-50 years. Tissue samples consisted of 25-mg tissue blocks. Dissociation of the human adipose tissues was immediately processed (within 3 h of removal from the patients) without snap-frozen or cryo-preservation.

METHOD DETAILS

scRNA-seq Library Preparation

scRNA-seq libraries were generated using the Chromium Single Cell 3′ Library & Gel Bead Kit (PN-1000092, 10X Genomics), Chromium Single Cell B Chip kit (PN-1000074, 10X Genomics), and Chromium i7 Multiplex Kit (PN-120262, 10X Genomics). Cells were resuspended in reverse transcription enzyme mix and loaded onto the Chromium Single Cell B Chip to generate gel beads-in-emulsion of 6,000 cells per channel. Reverse transcription was performed using a Bio-Rad C1000 Thermal Cycler. cDNA purification and library generation were performed according to the manufacturer's instructions. Libraries were sequenced on an Illumina NovaSeq 6000 instrument (paired-end 100-bp reads), with an average of 50,000 read pairs per cell.

scRNA-seq Data Processing

Raw reads were mapped to a mouse reference genome (GRCm38) using the Ensembl GRCm38.95 GTF file and the Cell Ranger software (v3.0.2). For each sample, a gene-by-cell count matrix was generated with default parameters, except for expected cells = 6000. Using the emptyDrops function of the DropletUtils (v1.6.1) R package (Lun et al., 2019) with a false discovery rate (FDR) < 0.01, empty droplets were removed. To filter out low-quality cells, cells with > 5% (EAT NCD, EAT 10-week HFD, and IAT NCD) or > 3% (EAT 2-week HFD, IAT 2-week HFD, IAT 10-week HFD) of unique molecular identifiers (UMIs) assigned to mitochondrial genes, < 1,000 total UMI counts, or < 1,000 detected genes were excluded using the calculateQCMetrics function of the scater (v1.14.6) R package (McCarthy et al., 2017). To normalize cell-specific biases, cells were clustered using the quickCluster function of the scran (v1.14.6) R package (Lun et al., 2016). Then, cell-level size factors were calculated using the computeSumFactors function of the same package. Raw UMI counts were normalized by size factors and then log2-transformed with a pseudocount of 1.

Highly variable genes (HVGs) were identified using the modelGeneVar function of the scran package, with FDR < 0.05 for biological variability. All cells across the fat depot and diet conditions were clustered into 17 clusters using the FindClusters function of the Seurat (v3.2.3) R package (Stuart et al., 2019) on the first 15 principal components (PCs) of HVGs with resolution = 0.8. Cells were visualized in a two-dimensional UMAP plot using the RunUMAP function of the same package. Two clusters (clusters 14 and 16) annotated as immune cells and mesothelial cells were removed. Cells from EAT samples were further clustered using the method described above with the top 10 PCs. Cluster 12, annotated as testis cells, was removed. All remaining cells were visualized in the UMAP plot from the top 15 PCs. Cells in the normal chow diet were grouped into 11 clusters and visualized in the UMAP plot using the above method, with the top 25 PCs of 1,000 HVGs.

scRNA-seq Data Analysis

Stage-specific marker genes were identified using the FindAllMarkers function of the Seurat package, with default parameters. Pseudotime analysis was performed for each condition using the run_palantir function of the Palantir (v0.2.6) python package (Setty et al., 2019). For Palantir t-SNE plots in EAT or IAT NCD, diffusion components (DCs) were computed using the run_diffusion_maps function with the first 200 PCs for EAT NCD and the first 100 PCs for IAT NCD. Then, a k-nearest neighbor (k-NN) graph (k = 30) was constructed from the first 10 DCs. The coordinates for the t-SNE plots were computed using the run_tsne function with perplexity = 300 (for EAT NCD) or 200 (for IAT NCD). Gene ontology analysis was performed using the runTest function of the topGO (v2.38.1) R package. For Palantir t-SNE plots in the EAT and IAT samples, batch effects across diet conditions were corrected using the run_harmony function of the Harmonypy (v0.0.4) Python package on 300 PCs (Korsunsky et al., 2019). Then, a k-NN graph (k = 30) was constructed from the first 10 DCs. The coordinates for the t-SNE plots were computed using the run_tsne function with perplexity = 400 (for EAT) or 300 (for IAT). To identify differentially expressed genes (DEGs) between the two fates, cells from EAT samples were grouped into early (0–0.35), intermediate (0.35–0.75), or late (0.75–1), according to their pseudotime. Cells were assigned into one of two differentiation fates by binomial sampling based on branch probabilities, which were calculated for each cell using the run_palantir function. DEGs between the two fates were identified for each pseudotime stage (early, intermediate, and late) using the FindAllMarkers function of the Seurat package. Signaling pathway activity for each cluster was inferred using the progeny function of the progeny (v1.12.0) R package (Schubert et al., 2018). For Monocle2 trajectory analysis, batch effects across diet conditions were corrected using the reduceDimension function of the monocle2 (v2.14.0) R package (Qiu et al., 2017), regressing out the number of total UMIs and detected genes. To project EAT NCD cells onto IAT NCD cells, k-NNs (k = 10) of each EAT NCD cell were obtained from IAT NCD cells with respect to the Pearson correlation coefficients of normalized expression profiles of HVGs between EAT and IAT NCD cells, by applying the knn.index.dist function of the KernelKnn (v 1.0.8) R package. For every EAT NCD cell, two-dimensional coordinates of 10-NNs in the t-SNE plot of IAT NCD cells were averaged to obtain the projection of the EAT NCD cell. Cells from IAT and EAT NCD samples were also integrated using the RunHarmony function of the harmony (v1.0) R package on the top 15 PCs of HVGs. The corrected PCs were used as inputs for clustering and visualization.

Adipose Tissue Fractionation

EAT and IAT were obtained from age-matched NCD-fed and 2- or 10-week HFD-fed mice. Adipose tissues were fractionated as described previously (Jeon et al., 2020). Briefly, adipose tissues were minced and digested with collagenase buffer [0.1 M HEPES, 0.125 M NaCl, 5 mM KCl, 1.3 mM $CaCl_2$, 5 mM glucose, 1.5% (w/v) bovine serum albumin, and 0.1% (w/v) collagenase I (Worthington, 49A18993)] in a shaking water bath at 37°C for 30–60 min. After centrifugation at 200 × *g*, room temperature (RT) for 5 min, the pelleted stromal vascular fraction (SVF) was collected. The SVF was incubated in red blood cell lysis buffer (1.7 M Tris, pH 7.65, and 0.16 M NH_4Cl) for 15 min. Then, the SVFs were washed with phosphate-buffered saline (PBS) several times, passed through a 100-μM filter (93100, SPL), and collected by centrifugation at 200 × *g* for 5 min.

Fluorescence-Activated Cell Sorting (FACS)

FACS was carried out as previously described (Sohn et al., 2018b), with minor modifications. SVFs were stained with anti-CD31 (1:100, 102405, 102409 and, 102419 BioLegend), anti-CD45 (1:100, 103107, 103111, and 103131, BioLegend), anti-DPP4 (1:100, 137809, BioLegend), anti-ICAM1 (1:100, 116107, BioLegend), anti-SDC1 (1:100, MA5-23527, Thermo Fisher), anti-CD9 (1:100, 124811, BioLegend) and anti-BST2 (1:100, 127015, BioLegend) for 30 min. To detect $Ki67^+$ cells, the SVFs were co-stained with anti-Ki67 (1:100, 151211, BioLegend). The cells were analyzed using a FACS Canto II instrument (BD Biosciences).

Isolation of SVFs from Human Adipose Tissue

Human adipose tissues were rinsed in PBS twice, manually minced, and digested with collagenase buffer [0.1 M HEPES, 0.125 M NaCl, 5 mM KCl, 1.3 mM $CaCl_2$, 5 mM glucose, 1.5% (w/v) bovine serum albumin, and 0.1% (w/v) collagenase I (Worthington, 49A18993)] in a shaking water bath at 37°C for 30–60 min. The subsequent steps were the same as those for preparing mouse adipose tissue fractionation.

Immunocytochemistry and Immunohistochemistry

Samples were incubated with fluorescently labeled Hoechst 33342 (ab228551, Abcam) and stained with fluorescein isothiocyanate-conjugated BODIPY 493/503 (D3922; Thermo Fisher Scientific). BODIPY staining was performed as previously with minor modifications (Han et al., 2019). Adipogenesis was assessed by staining with BODIPY 493/503 (D3922, Invitrogen) for lipid droplet

accumulation and by staining with Hoechst 33342 for nucleus number at 8 days post induction (mouse cells) and 2 weeks post induction (human cells) in individual wells of a 384-well plate (37384, SPL). The cells were imaged using a CQ1 microscope (Yokogawa). Coherent anti-Stokes Raman scattering was used to measure lipids (Kong et al., 2020).

Whole-mount imaging was carried out as previously with minor modifications (Park et al., 2019). A small fraction of fat tissue was fixed in 4% paraformaldehyde for 10 min and permeabilized with 0.5% Triton X-100 in PBS for 5 min. The fixed tissues were incubated with a primary antibody against UCP1 (14670; Cell Signaling, 1:300) and a primary antibody against tyrosine hydroxylase (818007, BioLegend, 1:500) overnight. The tissues were then washed three times for 10 min each, incubated with secondary antibody for 1 h, washed three times for 5 min each, and mounted on slides in 8-well plates (155409, Nunc Lab-Tek II) with Hoechst 33342. Tissues were observed and imaged using a CQ1 microscope (Yokogawa).

For immunohistochemistry, small fractions of fat tissues were isolated from mice, fixed in 4% paraformaldehyde, and embedded in paraffin. The paraffin blocks were cut into 5-μm sections and stained with hematoxylin and eosin. Tissues were imaged using a digital slide scanner (Axio Scan Z1, Carl Zeiss).

Isolation of Adipocyte Nuclei

BrdU (559619, BD Biosciences) was administered in the drinking water at 0.8 mg/mL for one week. Adipocytes were fractioned using collagenase treatment. Floating adipocyte fractions were washed with collagenase buffer three times and centrifuged at 200 × *g* for 10 min. Isolation of intact adipocytes was verified by quantitative reverse transcription (RT-q)PCR analysis of adipocyte marker genes (*Adipoq*, *Plin1*), and endothelial cell marker gene (*Pecam1/CD31*), and a lymphocyte marker gene (*Ptprc/CD45*). *CD31* and *CD45* were expressed in the SVF, but not in the adipocyte fraction. Nuclei isolated from adipocyte fractions were processed using the FITC BrdU Flow Kit (559619, BD Biosciences) according to the manufacturer's instructions. Following antibody incubation, the samples were washed and analyzed using a FACS Aria II instrument (BD Biosciences). The proportion of $BrdU^+$ nuclei among total nuclei ($7\text{-}AAD^+$) was measured.

Cell Culture

ASCs were cultured at 37°C and 5% CO_2 in a humidified cell incubator. ASCs were seeded in 96-well plates at 3,000 cells/well and cultured in Dulbecco's modified Eagle's medium (DMEM) containing 10% FBS for two days until confluence. For adipogenic differentiation, the cells were incubated in adipogenic media (1 μM dexamethasone, 520 μM methylisobutylxanthine, 850 nM insulin, and 1 μM rosiglitazone). Two days after adipogenic induction, the culture medium was replaced with FI medium (850 nM insulin and 1 μM rosiglitazone), and the cells were analyzed after 8–10 days of differentiation (Lee et al., 2018). For osteogenic differentiation, cells were cultured in DMEM with 10% FBS, 50 μM ascorbic acid, and 10 mM β-glycerophosphate for 10 days. For beige adipocyte differentiation, the cells were incubated in beige adipogenic media (1 μM dexamethasone, 520 μM methylisobutylxanthine, 850 nM insulin, 1 nM T3, 125 μM indomethacin, and 1 μM rosiglitazone) (Lee et al., 2018). After adipogenic induction for two days, the culture medium was replaced with FI medium (850 nM insulin, 1 nM T3, and 1 μM rosiglitazone), and the cells were analyzed after 8–10 days of differentiation.

Cell Proliferation Assay

Cell proliferation was assayed as described previously (Lee et al., 2017) with minor modifications. Briefly, cells were seeded in 96-well plates at 100 cells/well. CCK-8 (Dojindo, CK04) assays were performed according to the manufacturer's instructions. For cell proliferation assay using CM, adipocytes and SVFs were isolated from IAT and EAT of NCD- and 3-day HFD-fed mice. Adipocytes and SVFs were incubated in DMEM containing 10% FBS for 24 h and CM was collected. Both adipocytes CM and SVF CM were normalized by fat mass (5 mL of media per adipocytes and SVFs from 1 g of fat tissue).

Monocyte Migration Assay

In vitro monocyte migration was performed using THP-1 monocytes. For CM preparation, chopped fat tissues or IAT ASCs were incubated in serum-free DMEM for 24 h and CM was harvested. CM from fat tissue was normalized by fat mass (5 mL of media per 1 g of fat tissue). Synthetic CXCL12 or CXCL14 peptides were dissolved in serum-free DMEM. In CM experiments. THP-1 cells were pre-stained with 2 μM of CellTracker-Red CMTPX (C34552; Thermo Fisher Scientific) to distinguish THP-1 cells and cells from CM. In each sample group, 2×10^5 (per well of the 6-well culture plate) or 5×10^4 (per well of the 24-well culture plate) THP-1 cells were loaded on the surface of the upper layer of Trans-well insert. 4 ∼12 h after incubation, the upper layer and Trans-well insert were carefully removed. Migrated THP-1 cells were stained with Hoechst dye (H3570; Thermo Fisher Scientific) and quantified using the CQ1 confocal microscope.

In vivo monocyte infiltration was performed using GFP^+ blood mononuclear cells. To isolate blood mononuclear cells from GFP-Tg mice, blood was collected by heart puncture and mixed with 20 μL of 0.5 M EDTA. Blood samples were pooled in a Greiner Leucosep tube (GN163290, Sigma Aldrich) pre-equilibrated with 3 mL of NycoPrep 1.077 (1114550, Axis-Shield PoC AS). After centrifugation at 2,500 rpm for 10 min, the middle layer was carefully isolated and washed with RoboSep buffer (20104, STEMCELL Technologies). Mononuclear cells in RoboSep buffer were intravenously injected into mice. 1 day after GFP^+ blood mononuclear cell injection, fat tissues were subjected to FACS analysis.

siRNA Treatment

siRNAs were purchased from Bioneer (Daejeon, South Korea). Cells were mixed with siRNA or vectors and transfected with a single pulse of 1100 V for 30 ms using a Microporator MP-100 (Digital Bio, Seoul, Korea) according to the manufacturer's instructions. Sequence information for the siRNAs is provided in Table S1.

RT-qPCR

Total RNA was isolated using Direct-zol RNA MiniPrep (Zymo Research). The RNA was reverse-transcribed using the ReverTra Ace qPCR RT Kit (Toyobo). RT-qPCRs were run using SYBR Green master mix (DQ384-40 h, Biofact). Target gene expression levels were normalized to *Tbp* expression. Primer sequences are listed in Table S1.

Transplantation and Lymph Node (LN) Dissection

$DPP4^+/GFP^+$ ES1 and IS1 ASCs were purified (donor cells) by FACS from EAT and IAT of GFP-Tg adult male mice. GFP^+ and $DPP4^+$ S1 cells were concentrated to ~5,000 cells/μl by centrifugation and then mixed 1:1 with Matrigel (356230, Corning) on ice. Donor cells (10-20 μl) were injected into the fat pads of WT C57BL/6 adult male mice. Donor GFP^+ cells were harvested from the recipient animals 3 h or 10 days after transplantation and subjected to FACS analysis.

For the LN dissection experiment, the skin near the IAT was incised, and the LN was removed. One week after LN removal, the mice were exposed to a cold environment (6°C) for 4 or 7 days or treated with a dose of 1 mg/kg body weight of CL316,243 compound for 7 days.

QUANTIFICATION AND STATISTICAL ANALYSIS

Data are presented as the mean ± standard deviation (SD). *N*-values indicated in the figures refer to biological replicates. All data were tested for normal distribution with D'Agostino-Pearson omnibus normality test. If the data were not normally distributed, Mann-Whitney test was performed. Means of two groups were compared using a two-tailed Student's t test. Means of multiple groups were compared using one-way ANOVA followed by Tukey's post hoc test. Two independent variables were compared using two-way ANOVA followed by Sidak's multiple comparisons test. Statistical analyzes were performed using GraphPad Prism (GraphPad Software).